

Unsupervised Discovery of Extreme Weather Events Using Universal Representations of Emergent Organization

Adam Rupe,^{1,2,*} Karthik Kashinath,^{3,4} Nalini Kumar,⁵ and James P. Crutchfield^{6,†}

¹*Pacific Northwest National Laboratory, Richland WA, USA.*

²*Center For Nonlinear Studies, Los Alamos National Laboratory, Los Alamos NM, USA.*

³*NVIDIA Corporation, Santa Clara CA, USA.*

⁴*NERSC, Lawrence Berkeley National Laboratory, Berkeley CA, USA.*

⁵*Intel Corporation, Santa Clara CA, USA.*

⁶*Complexity Sciences Center, Department of Physics and Astronomy,
University of California Davis, Davis CA 95616, USA.*

(Dated: September 29, 2023)

Spontaneous self-organization is ubiquitous in systems far from thermodynamic equilibrium. While organized structures that emerge dominate transport properties, universal representations that identify and describe these key objects remain elusive. Here, we introduce a theoretically-grounded framework for describing emergent organization that, via data-driven algorithms, is constructive in practice. Its building blocks are spacetime lightcones that embody how information propagates across a system through local interactions. We show that predictive equivalence classes of lightcones—local causal states—capture organized behaviors and coherent structures in complex spatiotemporal systems. Employing an unsupervised physics-informed machine learning algorithm and a high-performance computing implementation, we demonstrate automatically discovering coherent structures in two real-world domain science problems. We show that local causal states identify vortices and track their power-law decay behavior in two-dimensional fluid turbulence. We then show how to detect and track familiar extreme weather events—hurricanes and atmospheric rivers—and discover other novel coherent structures associated with precipitation extremes in high-resolution climate data at the grid-cell level.

Emergent phenomena are often of primary interest in the study of complex systems, but disentangling the web of nonlinear interactions that give rise to them presents enormous challenges to traditional paradigms of scientific inquiry. Although the broad use of numerical models has significantly improved our ability to study nonlinear systems, difficulties remain. The scale and complexity of model outputs can be such that they are now essentially as difficult to understand as the natural phenomena they approximate. That is, the challenge of uncovering the physical and causal mechanisms of emergent phenomena in a large-scale numerical model can be comparable to doing so in the natural system itself.

It is well known that emergent *coherent structures* dominate transport in nonequilibrium systems [1]. While they have clear impacts on transport, these organized structures themselves are often subtle and difficult to identify. A myriad of algorithms have been proposed, based on various *principles of organization*, that attempt to extract coherent structures directly from data. Proper orthogonal decomposition (POD) [2] and Koopman mode decomposition [3] are standard choices for time-independent flow dynamics in the Eulerian frame. Due to these restrictions, however, they are incapable of identifying and tracking localized structures that evolve through time. Lagrangian methods for time-dependent flows are thus preferred, but there are still many competing Lagrangian organizational principles [4].

The theories underlying most Lagrangian methods are mathematically involved and the associated data-driven

algorithms are costly and do not scale well to large problems. In addition, their organizational principles may not always capture the structures of interest to domain scientists. This results in a disconnect between developing general principles of organization and deploying data-driven algorithms in practice by domain scientists striving to detect coherent structures. Due to this, domain practitioners fall back on automated heuristics that are specialized to domain-specific problems.

As a prime example, consider the Earth system—a quintessential complex system [5, 6]. The emergent behaviors associated with climate change present one of the most pressing issues of our time [7]. Many of the direct impacts of climate change on society are felt through emergent organization in the form of *extreme weather events* [8], such as hurricanes and atmospheric rivers (AR). Moreover, as the Earth warms, the character of localized extreme weather events (EWE) has and will continue to change [9, 10].

Global climate models are the primary tool used by scientists to study EWEs and climate change more generally [11, 12]. While high-resolution models produce EWEs under a variety of warming scenarios, discovering the underlying mechanisms driving specific shifts in intensity, duration, and spatial dynamics of individual events is under active investigation by researchers. Large-scale surveys of various models and warming scenarios [13] are thus essential to study statistical changes in EWE behaviors, but detailed assessment is made difficult due to the sheer quantity of data produced. For example, CMIP 6

is estimated to contain 15-30 PB of total climate data [14]. There is an immediate need in the climate community for automated discovery and tracking of EWEs to better understand and predict how they are changing in a warming world and to help mitigate their deleterious impacts. Discovering EWEs in a principled, robust, and scalable manner remains an outstanding challenge.

Current practice in the climate community employs automated heuristics based on meteorological properties (e.g., temperature and pressure thresholds) to identify EWEs from data [15, 16]. In addition to being somewhat ad hoc, these heuristics are specialized to particular types of structure they identify. The heuristics used to identify hurricanes, for example, differ from those used to identify ARs. More worrying, hurricane heuristics used in one climate model may differ from those used in another—with, say, higher resolution. At best, this makes comparing EWE behavior across climate change scenarios challenging. In addition, the changing climate itself may lead to qualitatively different EWE behavior that eludes current heuristics.

In machine learning terminology, identifying individual events at the single-pixel or model-grid-cell scale is known as a *segmentation* analysis of extreme weather events. At first glance, EWE detection and tracking may seem an ideal use case for deep learning algorithms that have brought dramatic advances in computer vision. Indeed, there is considerable effort devoted to extreme weather segmentation using deep learning [17–20].

Deep learning’s main weakness, though, is that neural networks have been most successful at *supervised* computer vision tasks. In this, the networks are trained on *ground truth* labeled examples—data exemplars typically labeled by human experts. As with general fluid vortices [21], no ground truth is available for extreme weather events; see, e.g., Refs. [15, 16]. More to the point, *there is no generally agreed upon objective definition of an extreme weather event*. They are currently identified on a “know it when you see it” basis. For supervised deep learning, the automated heuristics implemented in the TECA code base [22] are used as surrogate “ground-truth” training examples, but the neural networks’ high evaluation scores show that they merely learn to reproduce the output of these heuristics. More recent efforts have turned to curated collections of expert-labeled images for training [23]. While more promising for practical application, this approach relies heavily on subjective human evaluation and not on a general organizational principle.

The absence of objective definitions of Lagrangian coherent structures and extreme weather events are symptomatic of a more general deficiency: *there is no objective definition of emergent organization*. Therefore, there is no objective way to evaluate any proposed organizational principle and associated unsupervised algorithms that discover structures as instances satisfying the prin-

ciple. The current recourse is to rely on subjective, and largely visual, intercomparison among competing principles [4]. In addition, there is a larger question of whether or not there is a *single* principle that can capture the wide array of organized structures produced in complex spatially-extended dynamical systems.

The following answers this question by proposing *the local causal states as universal representations for emergent organization*. With foundations in complex systems theory and the physics of self-organization [24, 25], the local causal states decompose a system’s behavior into minimal, causally-interacting components. An organizational principle using (deviations from) hidden spacetime symmetries revealed by the local causal states is able to extract coherent structures in cellular automata models [26] and Lagrangian coherent structures in complex fluid flows [27].

Here, we report on two contributions towards a universal and actionable organizational principle using the local causal states: (i) A quantitative verification method for coherent structure discovery that identifies the non-stationary power-law relaxation of vortex dynamics in two-dimensional free-decay turbulence. And, (ii) a global extreme weather event segmentation in high-resolution general circulation model (GCM) data. Beyond known EWEs—such as, hurricanes and atmospheric rivers—we demonstrate that the local causal states extract novel structures associated with precipitation extremes.

Local Causal States

We now introduce our organizational principle and compare it with two other general approaches to structure detection—proper orthogonal decomposition and finite-time coherent sets. True to their name, the *local causal states* are defined using a weak notion of causality. Not only does the future follow from the past, but in spatiotemporal systems that evolve through local interactions, there is a limit on how fast causal influence can propagate. This limit defines *lightcones* in the system that are essential features used in constructing local causal states. The *past lightcone* (L^-) of a point in spacetime is the collection of all points at previous times that could possibly have influenced the spacetime point through the local interactions. Similarly, the *future lightcone* (L^+) of a spacetime point is the collection of all points at later times that the spacetime point could influence through local interactions.

Local causal states are then defined through the *local causal equivalence relation*: two past lightcone configurations, denoted ℓ^- , are considered causally equivalent, denoted \sim_ϵ , if they have the same distribution over co-occurring future lightcones (see Figure 1):

$$\ell_i^- \sim_\epsilon \ell_j^- \iff \Pr(L^+ | L^- = \ell_i^-) = \Pr(L^+ | L^- = \ell_j^-) .$$

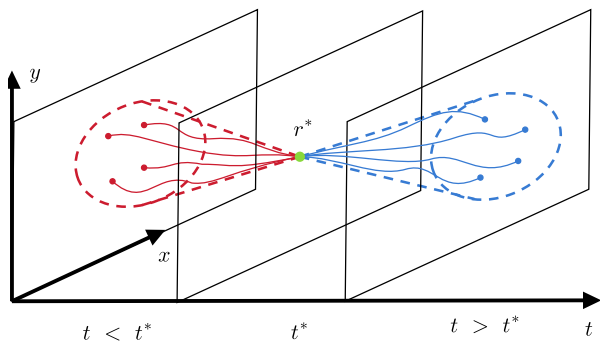


FIG. 1. Co-occurring past (red) and future (blue) Lagrangian lightcones at spacetime point (r^*, t^*) shown with dashed lines. All possible Lagrangian trajectories (examples shown by solid lines) leading to and emanating from (r^*, t^*) are contained within the lightcones.

The local causal states are the equivalence classes of the local causal equivalence relation. A given local causal state is a set of past lightcone configurations that have the same distribution over co-occurring future lightcones [26]. This is expressed functionally by the map $\epsilon(\cdot)$ from past lightcone configurations to a local causal state: $\epsilon(\ell_i^-) = \epsilon(\ell_j^-)$ if and only if ℓ_i^- and ℓ_j^- belong to the same local causal state.

Crucially, the ϵ -function provides a pointwise mapping from points in spacetime to corresponding local causal states, through their past lightcones. When applied to all points in a spacetime field $X(\mathbf{r}, t)$ this produces a corresponding *local causal state field*, denoted $S(\mathbf{r}, t) = \epsilon(X(\mathbf{r}, t))$. Since $\epsilon(\cdot)$ is a pointwise mapping, applying at each point in spacetime, the resulting local causal state field $S(\mathbf{r}, t)$ shares the same coordinate geometry as its associated spacetime field $X(\mathbf{r}, t)$.

This means the local causal states provide a *space-time segmentation*, as desired. That is, the finite set $\mathcal{S} = \{S_i\}$ of local causal states can be thought of as a set of `class labels` S_i and each point in spacetime is assigned one of these local causal state labels through the ϵ -function. Since the ϵ -function is a local mapping defined using lightcones, it is *equivariant* under spacetime translations, rotations, and reflections. This guarantees that the local causal state representations do not depend on spacetime location or orientation of structures they extract.

Data-driven approximation of the ϵ -function is achieved using two stages of clustering [27]. The first clustering stage γ is a distance-based partitioning of the space of finite-depth past lightcones, which we implement using the K-Means algorithm [28]. The γ -function maps past lightcones to their associated distance-based cluster. Performing distance-based clustering on past and future lightcones creates sets of cluster labels so that the distributions $\Pr(\gamma(L^+) | \gamma(\ell^-))$ can be empirically approxi-

mated through simple counting. During the second clustering stage ψ , elements of the γ -partition are clustered together if they have approximately the same empirical future-lightcone distribution $\Pr(\gamma(L^+) | \gamma(\ell^-))$. Elements of the γ -partition are mapped to their resulting clusters under the ψ -function. The approximated ϵ -function used for inference is thus given as:

$$\epsilon(\ell^-) \approx \psi(\gamma(\ell^-)) .$$

Systems under study often have multiple physical fields of interest; in the climate domain these include temperature, pressure, wind speeds, and water vapor. In these multivariate cases, the spacetime fields and lightcones extracted from them are tensors, with each point in spacetime having a vector of values over the multiple physical fields. Multivariate local causal state analysis is performed using a tensor lightcone metric that computes distances for the γ -partition using values from multiple physical fields. Using this tensor lightcone metric, the local causal states may be tuned to the specific physics of the system. See the Supplementary Materials for more details on the local causal states and their data-driven reconstruction.

At present, the canonical representation learning method for spatiotemporal systems is the proper orthogonal decomposition (POD) [2]. In this, a fixed set of spatial modes are found that provide an optimal reconstruction of the spatiotemporal system through linear superposition using time-varying coefficients.

POD modes, also called Empirical Orthogonal Functions in the climate literature, are the learned representations from which we may extract potential coherent structures. The local causal states can be seen as a representation learning method similar to POD, in that it learns a finite set of “template” representations. However, rather than learning full spatial field templates (modes), the local causal state templates are localized and assigned at each point in space and time. This greatly increases their representational capacity compared to POD modes, as they can be arranged arbitrarily in space and time.

Since POD modes are spatially global (Eulerian) and fixed in time, they are structurally very limiting and are incapable, for instance, of tracking the evolution of spatially-localized structures over time. Lagrangian methods are thus better suited for coherent structures that dominate material transport in fluid flows. The Lagrangian approach most similar to the local causal states are the *finite-time coherent sets* [29, 30] that identify contiguous regions in space at a given time such that the points in that region mostly evolve together (coherently) under the Lagrangian flow. Most simply, they are estimated as eigenfunctions of the time-dependent Perron-Frobenius operator (defined from the Lagrangian flow map) with eigenvalues close to unity.

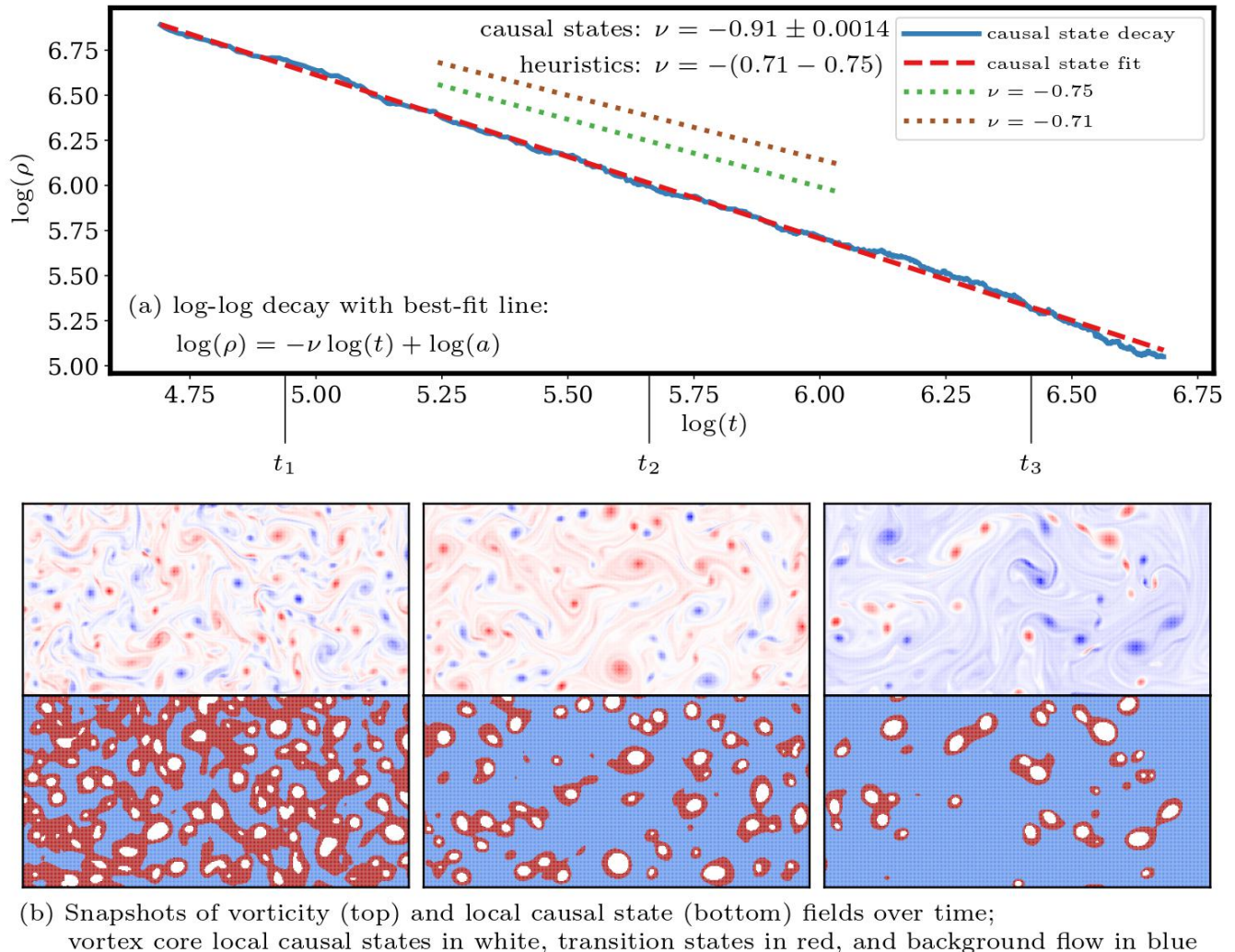


FIG. 2. Local causal state vortex cores over time and their power law decay.

Noting the importance of Lagrangian dynamics for coherent structures in fluids, we use *Lagrangian lightcones* when constructing local causal states of fluid flows. Rather than tracking information propagated through local interactions, Lagrangian lightcones track information propagated through advection. Specifically, all possible Lagrangian trajectories that could lead to (from) a point in spacetime are contained within its past (future) Lagrangian lightcone, as shown in Figure 1.

The collectively-evolving bundles of trajectories identified as coherent sets produce a distinct signature in the lightcones of points in the set. Therefore coherent sets correspond to a distinct set of local causal states. Similarly, the boundaries of coherent sets are hyperbolic Lagrangian coherent structures that act as transport barriers. As observed in Ref. [27], hyperbolic Lagrangian coherent structures also correspond to boundaries of local causal states. The transport barrier produces distinct

lightcone signatures on either side, resulting in two different local causal states across the boundary.

Vortex Decay in Two-Dimensional Turbulence

Lacking an objective definition of coherent structures, how does one evaluate proposed organizational principles and their ability to identify structures from data? As mentioned above, qualitative visual comparison is typical. In Ref. [27] local causal states are visually compared to other Lagrangian methods assessed in Ref. [4], with good agreement between the local causal states and the leading Lagrangian methods for identifying vortices specifically. Here, though, we go further to *quantitatively* evaluate coherent structure identification using the local causal states' ability to capture nonstationary behavior, including coherent structures with finite lifespans.

We demonstrate this by analyzing a longstanding problem in hydrodynamics—vortex detection in two-dimensional free-decay turbulence [31]. Like-signed vortices—the coherent structures of interest—undergo pairwise annihilation. This results in a nonstationary decay behavior with a power-law decay rate:

$$\rho(t) = a t^{-\nu} , \quad (1)$$

where $\rho(t)$ is the number of vortices and ν is the vortex decay rate. Empirically, ν is observed to be $\nu \sim 0.71 - 0.75$ [31, 32]. Extracting the decay rate provides an opportunity for a quantitative comparison with known physical behavior.

Recall that domain scientists employ heuristics specialized to their particular problem, rather than general organizational principles, to identify their structures of interest. The power-law decay and the range of accepted decay rates in two-dimensional turbulence are identified using tailored vortex heuristics based on vorticity thresholding along with geometric considerations [31].

The local causal states are able to identify vortices in the two-dimensional turbulent flow using a general organizational principle: *coherent structures are spatially-localized and temporally-persistent deviations from space-time symmetries in the local causal state field* [26]. Local causal state segmentation distinguishes between vortices spinning in different directions, but estimating the decay rate requires tracking only the total number of vortices. Therefore, segmentation is performed on the absolute value of vorticity, resulting in three local causal state class labels, as Figure 2 (b) shows. These labels can be qualitatively interpreted as the background potential flow (blue), vortex cores (white), and transition regions (red) surrounding the vortex cores [31]. The background potential flow state acts as the hidden spacetime symmetry that is broken locally by the vortex states.

Quantitative analysis comes from algorithmically counting the number of vortex cores at each time using a union-find algorithm [33]. A log-log plot of the number of vortex cores over time is shown in Figure 2 (a). Since the decay rate is a power law, the log-log plot is linear, with the decay rate ν given as the slope. Note though that we fit the power law in Eq. (1) directly using `scipy.optimize.curvefit`; a log-log plot is shown in Figure 2 (a) for visual clarity.

The (log-log) best-fit line shows the decay rate of local causal state vortex cores over time fits very well to a power law, with decay rate $\nu \approx 0.91$. Slopes representing the accepted empirical range $\nu = -(0.71 - 0.75)$ are shown for comparison. As seen in the full spacetime segmentation video [34], the higher-than-expected decay rate is due to a small number of vortex core states eventually being mislabeled as background, and so they vanish without pairwise merging. However, the overall behavior is dominated by the correct physical mechanism of pair-

wise vortex merging, giving a strong fit to the power law decay.

We note that finite-time coherent sets are the only other Lagrangian method able to capture the nonstationary birth and death of individual structures over time [35]. However, the required mathematics is quite complicated. Whereas, the ephemeral behavior of structures with finite lifespans is naturally encapsulated by the local causal states without additional modification. It remains to be seen if the Lagrangian finite-time coherent set algorithm can scale to larger problems and reproduce quantitative relationships like the vortex decay just described.

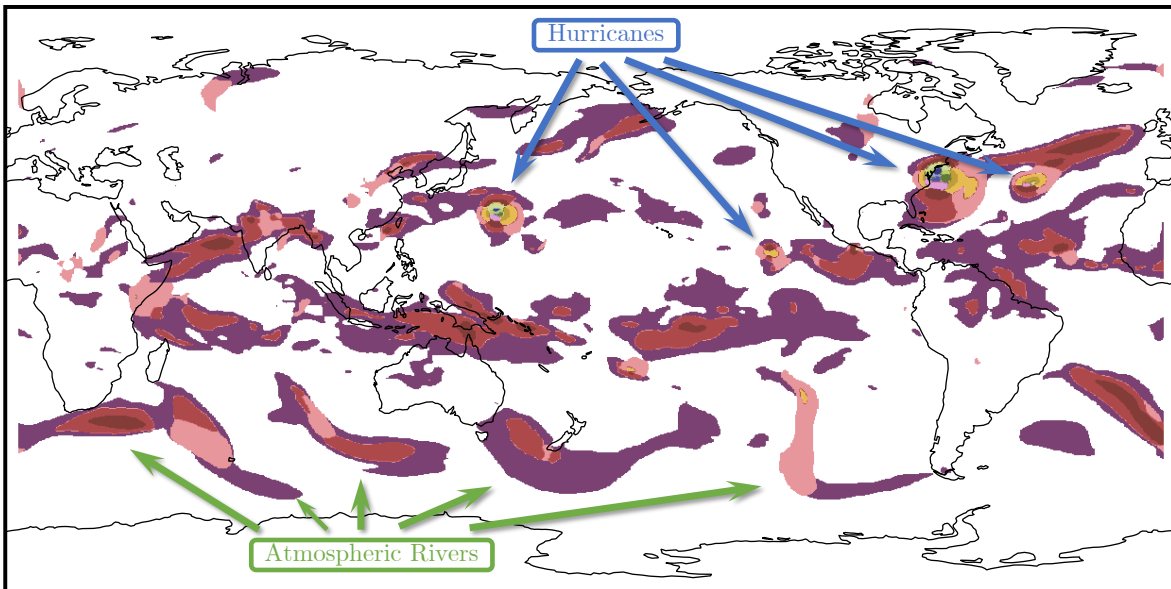
Discovering and Tracking Extreme Weather Events

Employing data from the 0.25-degree CAM5.1 Global Circulation Model [36] the following analyzes extreme weather events in global climate data. The goal of our analysis is twofold: (i) simultaneously identify known structures, such as hurricanes and ARs, using a general and robust organizational principle (rather than specialized heuristics or supervised deep learning), and (ii) explore as-of-yet undiscovered structures and their relevance for precipitation extremes. The physics of EWEs is incorporated into the local causal states through multivariate segmentation using wind velocities and column-integrated water vapor. This approach is based on the integrated vapor transport (IVT) field, commonly used by climate scientists to study EWEs [37].

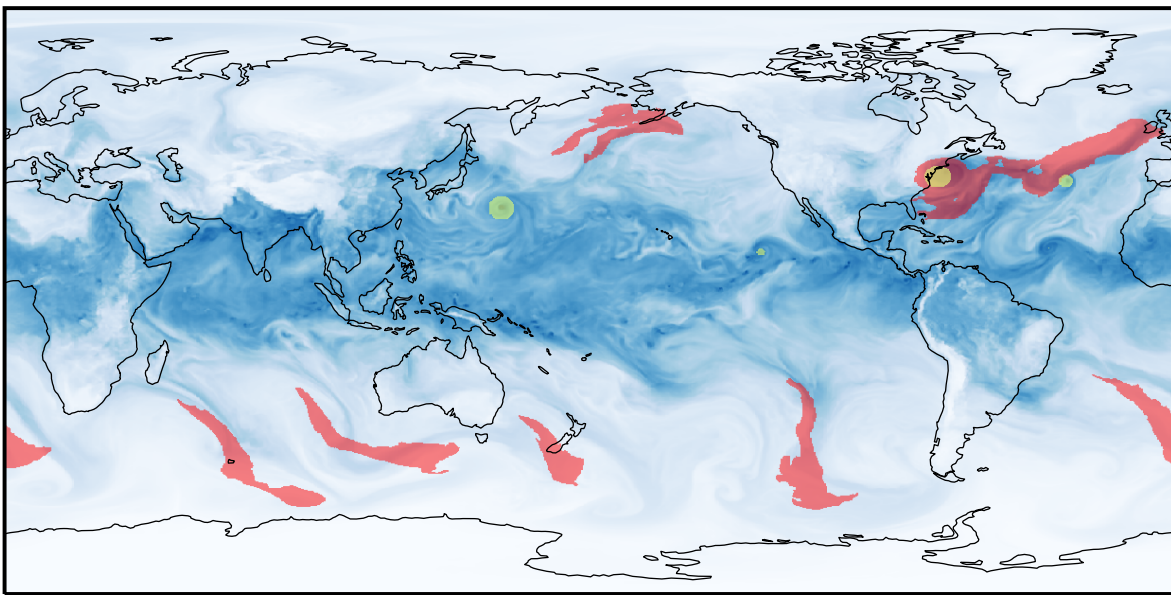
Performing a univariate segmentation on the scalar IVT field itself, we find a set of local causal states that visually coincide with hurricanes. That is, local causal states in this `hurricane` set (almost) only occur in spacetime locations where a hurricane is present. Using the shared coordinate geometry, we can then create an unsupervised hurricane tracker by simply highlighting spacetime points where these `hurricane` states occur. A snapshot of this tracker and its construction is shown in Figure S3 in the Supplementary Information. The full spacetime video of this hurricane tracker can be seen in [38].

Atmospheric rivers are more difficult to isolate with a unique set of AR states from a similar IVT field segmentation. However, the more general extreme weather segmentation we now describe does encompass ARs, along with other EWE coherent structures.

In contrast to conforming the local causal state analysis with known EWE structures as above (which, recall, are not objectively defined), we now turn to novel EWE structure discovery. Following the local causal state coherence principle of localized structures breaking a hidden spacetime symmetry, we seek to identify sets of local causal states breaking a uniform background state, similar to the blue background state for turbulent vortices shown in Figure 2 (b). Such a background state is not re-



(a) Local causal state EWE segmentation



(b) TECA AR (red) and hurricane (yellow) segmentation

FIG. 3. Hurricane segmentation masks created from local causal state segmentation of the IVT field.

covered using a univariate segmentation of the IVT field nor the integrated vapor field; see Figure S3 (a).

A uniform background symmetry state is recovered, however, using a multivariate segmentation with the tensor lightcone metric given by Equation (S11) in the Supplementary Information. Motivated by the construction of the IVT field, this multivariate segmentation utilizes

the column-integrated water vapor field, and the two component fields of mid-column wind velocity. A snapshot of the local causal state field from this multivariate segmentation is shown in Figure 3 (a). Video of a general EWE tracker, similar to the hurricane tracker above, using these local causal states is seen in [39]. The uniform background local causal state is colored white, with all

other colors then corresponding to coherent structures identified by the local causal state definition.

We label the nonbackground local causal states as **EWE** states since they simultaneously encompass hurricanes and atmospheric rivers. To justify this statement, we include a comparison with the TECA hurricane [22] and AR [40] heuristics on the same dataset, shown in Figure 3 (b) overlaid on top of the integrated water vapor field. TECA and the similar TempestExtremes [41] are the state-of-the-art software packages that implement extreme weather segmentation heuristics used in practice by climate scientists.

Visually, we can see in Figure 3 that **hurricane** (yellow) and **AR** (red) structures identified by TECA in (b) are encompassed by **EWE** local causal states in (a). Quantitatively, 82% of spacetime points in the dataset identified as either **hurricane** or **AR** by TECA are also identified as **EWE** by the local causal states. Recall that TECA and related heuristics are *not* ground-truth for these structures, and so it is not necessarily desirable for the local causal states to cover 100% of the TECA segmentation points. In fact, in our dataset the TECA AR heuristics have a false positive signal that identifies a hurricane as an AR, as confirmed by the author of the TECA AR heuristics in personal communication; see Figure S4 in the Supplementary Information.

In addition to the known hurricane and AR structures, there are many additional coherent structure signatures in the local causal state segmentation that do not correspond to known extreme weather events. To test their significance, we investigate the co-occurrence of precipitation extremes [42] with these **EWE** local causal states. That is, how many precipitation extremes occur in a spacetime location for which that same location in the local causal state field is an **EWE** state, rather than a **background** state?

	LCS	TECA
90 th percentile extremes		
global	45.0%	11.0%
tropics	61.7%	0.5%
extra-tropics	40.8%	23.3%
99 th percentile extremes		
global	58.1%	27.3%
tropics	69.5%	1.43%
extra-tropics	57.8%	43.3%
99.9 th percentile extremes		
global	75.3%	21.8%
tropics	76.7%	2.73%
extra-tropics	77.8%	51.3%

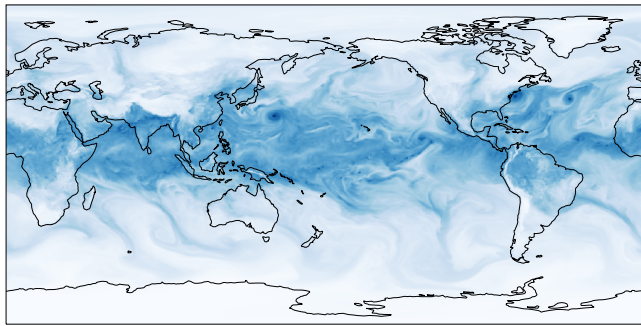
TABLE I. Percent of extreme precipitation events co-occurring with local causal state (LCS) and TECA segmentations.

Precipitation extreme results from the full three month time span of our climate dataset are shown in Table I, with analogous TECA results given for comparison.

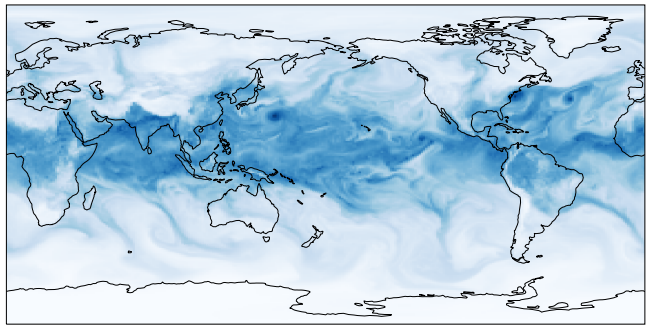
Three different percentile thresholds are given for defining the extremes, and for each case results are given globally, as well as broken down between tropics and extratropics. The zonal breakdown is given because the hurricane and AR structures identified by TECA are largely extratropical phenomena. (The TECA AR heuristics explicitly filter out potential signals in the tropics.) In all cases, the LCS **EWE** states capture a significantly larger proportion of precipitation extremes than the combined TECA segmentation. Given that 82% of the TECA segmentation is identified as **EWE** by the local causal states, this means the novel **EWE** coherent structures identified by the local causal states are significantly associated with precipitation extremes. Thus, we identify these coherent structures as novel extreme weather events discovered by the local causal states. Note that both the local causal state and TECA segmentations are created without any direct use of precipitation fields.

To close, we emphasize that the standard extreme weather segmentation paradigm [43] used by TECA and TempestExtremes heuristics are in the Eulerian framework, unlike the Lagrangian local causal states. The known shortcomings of Eulerian coherent structure segmentation [4] contribute, at least in part, to the inability of extreme weather heuristics to generalize across climate data. Crucially, hurricane and AR heuristics are not robust to the resolution of climate models [44]. In contrast, the general organization principle embodied by the local causal states is robust across model resolution, as demonstrated in Figure 4. We employed a 4x4 block-averaging (mean pooling) filter to reduced the resolution of our climate dataset fourfold, from 0.25 degree resolution to 1.0 degree. A local causal state segmentation was performed on this low-resolution data with the same parameters used in the high-resolution segmentation (except for the “speed of light” which is reduced because we are changing spatial resolution in the dataset without changing temporal resolution).

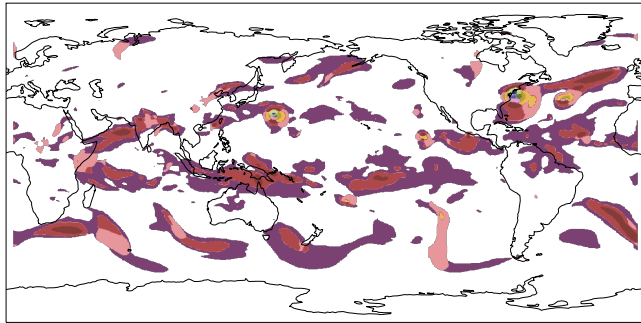
Visually, the resulting local causal state field is very similar to that from the high-resolution data. However, we note that the two segmentations and their local causal states are distinct and should not be directly identified. The 4x4 block averaging operation is incommensurate with the odd-length dimensions of the lightcone spatial slices. Thus, there is not a direct relation between the lightcones of the high- and low-resolution datasets, nor between their local causal states. Hence, we have kept distinct color labels of unique local causal states (assigned randomly by our algorithm) in Figure 4 (c) and (d). Importantly, though, the *segmentation semantics* of **background** and **EWE** are shared between the local causal states across resolutions.



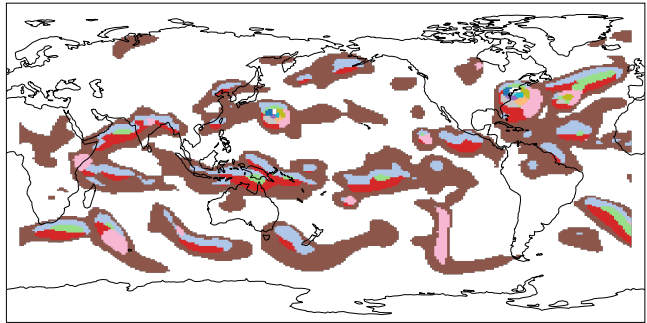
(a) High-resolution (0.25 degree) TMQ field



(b) Low-resolution (1.0 degree) TMQ field



(c) High-resolution local causal state field



(d) Low-resolution local causal state field

FIG. 4. Snapshots of water vapor field from high- (a) and low-resolution (b) versions of our CAM5.1 data, with the corresponding local causal state field snapshots shown in (c) and (d), respectively.

Conclusions

Advances in dynamical systems and applied ergodic theory are forming the foundations of a new paradigm for data-driven science [45]. For example, it is now clear that data-driven and physics-based predictive models are intimately related [46]. Beyond predictive modeling, uncovering the underlying mechanisms behind emergent behaviors is a crucial component of scientific inquiry and remains an outstanding challenge. Physics-informed data-driven methods, like those introduced here, provide a promising new avenue in this [47, 48].

Motivated by local causality and the physics of organization encapsulated by causal equivalence, the local causal states provide universal representations for emergent organization in complex spatiotemporal systems. Our approximation algorithm and high-performance computing implementation make the local causal states actionable in practice on large-scale cutting-edge domain science problems. Here, we produced a quantitative verification of coherent structure detection by automatically counting vortices in free-decay two-dimensional turbulence and recovering the known-power law decay over time using the local causal states and their ability to cap-

ture nonstationary behavior. We then employed the local causal states for automated, fully-unsupervised extreme weather discovery and demonstrated their ability to extract both known and novel structures in global climate data. With further refinement, the local causal states may be able to additionally provide a scale for strength and intensity of identified extreme weather events [49].

Further improvements to our extreme weather discovery may include the extension to other climate variable inputs, such as potential vorticity [50]. Similarly, additional vertical structure in the input variables could be included. For example, the IVT field is integrated over full columns, whereas our IVT-inspired multivariate analysis utilizes wind fields from mid-column only. As described in detail in Ref. [27], our current HPC implementation is heavily memory bound, limiting the amount of input data. While the current implementation can scale to a large amount of input data on a large HPC system [27], scaling may be further improved in the future, for example with development of a streaming and distributed K-Means algorithm.

Taken all together, the local causal states bridge the gap between theoretically-motivated organizational principles and domain science applications, where they per-

form comparably to or even better than specialized heuristics catering to the particular problem on hand.

* adam.rupe@pnnl.gov

† crutchfield@ucdavis.edu

- [1] G. Haller, Lagrangian coherent structures, *Ann. Rev. Fluid Mech.* **47**, 137 (2015).
- [2] P. Holmes, J. Lumley, G. Berkooz, and C. Rowley, *Turbulence, Coherent Structures, Dynamical Systems and Symmetry* (Cambridge University Press, Cambridge, United Kingdom, 2012).
- [3] I. Mezić, Analysis of fluid flows via spectral properties of the koopman operator, *Annual Review of Fluid Mechanics* **45**, 357 (2013).
- [4] A. Hadjighasem, M. Farazmand, D. Blazeovski, G. Froyland, and G. Haller, A critical comparison of Lagrangian methods for coherent structure detection, *Chaos* **27**, 053104 (2017).
- [5] M. Ghil and V. Lucarini, The physics of climate variability and climate change, *Rev. of Mod. Phys.* **92**, 035002 (2020).
- [6] A. R. Ravishankara, D. A. Randall, and J. W. Hurrell, Complex and yet predictable: The message of the 2021 Nobel Prize in physics, *Proc. Natl. Acad. Sci. USA* **119**, e2120669119 (2022).
- [7] H.-O. Pörtner, D. C. Roberts, H. Adams, C. Adler, P. Aldunce, E. Ali, R. A. Begum, R. Betts, R. B. Kerr, R. Biesbroek, *et al.*, *Climate change 2022: Impacts, adaptation and vulnerability* (IPCC Geneva, Switzerland, 2022).
- [8] M. K. Tippett, Extreme weather and climate, *npj Climate and Atmospheric Science* **1**, 45 (2018).
- [9] M. J. Roberts, J. Camp, J. Seddon, P. L. Vidale, K. Hodges, B. Vannière, J. Mecking, R. Haarsma, A. Bellucci, E. Scoccimarro, L.-P. Caron, F. Chauvin, L. Terray, S. Valcke, M.-P. Moine, D. Putrasahan, C. D. Roberts, R. Senan, C. Zarzycki, P. Ullrich, Y. Yamada, R. Mizuta, C. Kodama, D. Fu, Q. Zhang, G. Danabasoglu, N. Rosenbloom, H. Wang, and L. Wu, Projected future changes in tropical cyclones using the CMIP6 HighResMIP multimodel ensemble, *Geophysical Research Letters* **47**, e2020GL088662 (2020).
- [10] A. Robinson, J. Lehmann, D. Barriopedro, S. Rahmstorf, and D. Coumou, Increasing heat and rainfall extremes now far outside the historical climate, *npj Climate and Atmospheric Science* **4**, 45 (2021).
- [11] P. N. Edwards, *A Vast Machine: Computer Models, Climate Data, and the Politics of Global Warming* (The MIT Press, 2010).
- [12] G. Flato, J. Marotzke, B. Abiodun, P. Braconnot, S. Chou, W. Collins, P. Cox, F. Driouech, S. Emori, V. Eyring, C. Forest, P. Gleckler, E. Guilyardi, C. Jakob, V. Kattsov, C. Reason, and M. Rummukainen, Evaluation of climate models, in *Climate Change 2013: The Physical Science Basis. Contribution of Working Group I to the Fifth Assessment Report of the Intergovernmental Panel on Climate Change*, edited by T. Stocker, D. Qin, G.-K. Plattner, M. Tignor, S. Allen, J. Boschung, A. Nauels, Y. Xia, V. Bex, and P. Midgley (Cambridge University Press, Cambridge, United Kingdom and New York, NY, USA, 2013).
- [13] V. Eyring, S. Bony, G. A. Meehl, C. A. Senior, B. Stevens, R. J. Stouffer, and K. E. Taylor, Overview of the Coupled Model Intercomparison Project Phase 6 (CMIP6) experimental design and organization, *Geoscientific Model Development* **9**, 1937 (2016).
- [14] M. Stockhause and M. Lautenschlager, CMIP6 data citation of evolving data, *Data Science Journal* **16** (2017).
- [15] U. Neu, M. G. Akperov, N. Bellenbaum, R. Benestad, R. Blender, R. Caballero, A. Cocozza, H. F. Dacre, Y. Feng, K. Fraedrich, J. Grieger, S. Gulev, J. Hanley, T. Hewson, M. Inatsu, K. Keay, S. F. Kew, I. Kindem, G. C. Leckebusch, M. L. R. Liberato, P. Lionello, I. I. Mokhov, J. G. Pinto, C. C. Raible, M. Reale, I. Rudeva, M. Schuster, I. Simmonds, M. Sinclair, M. Sprenger, N. D. Tilinina, I. F. Trigo, S. Ulbrich, U. Ulbrich, X. L. Wang, and H. Wernli, IMILAST: A community effort to intercompare extratropical cyclone detection and tracking algorithms, *Bulletin of the American Meteorological Society* **94**, 529 (2013).
- [16] C. A. Shields, J. J. Rutz, L.-Y. Leung, F. M. Ralph, M. Wehner, B. Kawzenuk, J. M. Lora, E. McClenny, T. Osborne, A. E. Payne, P. Ullrich, A. Gershunov, N. Goldenson, B. Guan, Y. Qian, A. M. Ramos, C. Sarangi, S. Sellars, I. Gorodetskaya, K. Kashinath, V. Kurlin, K. Mahoney, G. Muszynski, R. Pierce, A. C. Subramanian, R. Tome, D. Waliser, D. Walton, G. Wick, A. Wilson, D. Lavers, Prabhat, A. Collow, H. Krishnan, G. Magnusdottir, and P. Nguyen, Atmospheric river tracking method intercomparison project (ART-MIP): project goals and experimental design, *Geoscientific Model Development* **11**, 2455 (2018).
- [17] M. Mudigonda, S. Kim, A. Mahesh, S. Kahou, K. Kashinath, D. Williams, V. Michalski, T. O'Brien, and Prabhat, Segmenting and tracking extreme climate events using neural networks, in *DLPS Workshop, NeurIPS* (2017).
- [18] C. Jiang, J. Huang, K. Kashinath, Prabhat, P. Marcus, and M. Niessner, Spherical CNNs on unstructured grids, in *International Conference on Learning Representations* (2019).
- [19] T. Cohen, M. Weiler, B. Kicanaoglu, and M. Welling, Gauge equivariant convolutional networks and the icosahedral CNN, in *Proceedings of the 36th International Conference on Machine Learning*, Proceedings of Machine Learning Research, Vol. 97, edited by K. Chaudhuri and R. Salakhutdinov (PMLR, Long Beach, California, USA, 2019) pp. 1321–1330.
- [20] T. Kurth, S. Treichler, J. Romero, M. Mudigonda, N. Luehr, E. Phillips, A. Mahesh, M. Matheson, J. Deslippe, M. Fatica, Prabhat, and M. Houston, Exascale deep learning for climate analytics, in *Proceedings of the International Conference for High Performance Computing, Networking, Storage, and Analysis* (IEEE Press, 2018) p. 51.
- [21] B. Epps, Review of vortex identification methods, in *55th AIAA Aerospace Sciences Meeting* (2017) p. 0989.
- [22] Prabhat, O. Rübel, S. Byna, K. Wu, F. Li, M. Wehner, W. Bethel, *et al.*, TECA: A parallel toolkit for extreme climate analysis, in *Third Workshop on Data Mining in Earth System Science (DMESS)* (2012).
- [23] Prabhat, K. Kashinath, M. Mudigonda, S. Kim, L. Kapp-Schwoerer, A. Graubner, E. Karaismailoglu, L. Von Kleist, T. Kurth, A. Greiner, A. Mahesh, *et al.*, ClimateNet: an expert-labeled open dataset and deep

- learning architecture for enabling high-precision analyses of extreme weather, *Geoscientific Model Development* **14**, 107 (2021).
- [24] J. P. Crutchfield, Between order and chaos, *Nature Physics* **8**, 17 (2012).
- [25] A. Rupe and J. P. Crutchfield, Algebraic theory of patterns as generalized symmetries, *Symmetry* **14**, 1636 (2022).
- [26] A. Rupe and J. P. Crutchfield, Local causal states and discrete coherent structures, *Chaos* **28**, 1 (2018).
- [27] A. Rupe, N. Kumar, V. Epifanov, K. Kashinath, O. Pavlyk, F. Schlimbach, M. Patwary, S. Maidanov, V. Lee, Prabhat, and J. P. Crutchfield, Disco: Physics-based unsupervised discovery of coherent structures in spatiotemporal systems, in *2019 IEEE/ACM Workshop on Machine Learning in High Performance Computing Environments (MLHPC)* (IEEE, 2019) pp. 75–87.
- [28] D. Arthur and S. Vassilvitskii, K-Means++: the advantages of careful seeding, in *Proceedings of the eighteenth annual ACM-SIAM symposium on Discrete algorithms* (Society for Industrial and Applied Mathematics, 2007) pp. 1027–1035.
- [29] G. Froyland, K. Padberg, M. H. England, and A. M. Treguier, Detection of coherent oceanic structures via transfer operators, *Physical review letters* **98**, 224503 (2007).
- [30] G. Froyland, N. Santitissadeekorn, and A. Monahan, Transport in time-dependent dynamical systems: Finite-time coherent sets, *Chaos: An Interdisciplinary Journal of Nonlinear Science* **20**, 043116 (2010).
- [31] J. C. McWilliams, The vortices of two-dimensional turbulence, *J. of Fluid Mech.* **219**, 361 (1990).
- [32] G. F. Carnevale, J. C. McWilliams, Y. Pomeau, J. B. Weiss, and W. R. Young, Evolution of vortex statistics in two-dimensional turbulence, *Phys. Rev. Let.* **66**, 2735 (1991).
- [33] C. Fiorio and J. Gustedt, Two linear time union-find strategies for image processing, *Theoretical Computer Science* **154**, 165 (1996).
- [34] A. Rupe, 2D turbulence segmentation video, https://drive.google.com/file/d/1RoAh6J_gadhDcgWFPXa5z6g9q55TDM7G/view (2022).
- [35] G. Froyland and P. Koltai, Detecting the birth and death of finite-time coherent sets, *arXiv preprint arXiv:2103.16286* (2021).
- [36] M. F. Wehner, K. Reed, F. Li, Prabhat, J. Bacmeister, C.-T. Chen, C. Paciorek, P. Gleckler, K. Sperber, W. D. Collins, A. Gettelman, and C. Jablonowski, The effect of horizontal resolution on simulation quality in the community atmospheric model, CAM5.1., *J. of Modeling the Earth System* **06**, 980 (2014).
- [37] P. M. Sousa, A. M. Ramos, C. C. Raible, M. Messmer, R. Tomé, J. G. Pinto, and R. M. Trigo, North Atlantic integrated water vapor transport—from 850 to 2100 CE: Impacts on western European rainfall, *J. of Climate* **33**, 263 (2020).
- [38] A. Rupe, Hurricane tracker video, https://drive.google.com/file/d/11WxW0hNVL3eT1VHg0TcCBMdJQrbzrPLK/view?usp=share_link (2022).
- [39] A. Rupe, General EWE tracker video, https://drive.google.com/file/d/1mFnmHHLxK34IEVvMJA5axPNitVohMy9_/view?usp=share_link (2022).
- [40] T. A. O’Brien, M. D. Risser, B. Loring, A. A. Elbashandy, H. Krishnan, J. Johnson, C. M. Patricola, J. P. O’Brien, A. Mahesh, Prabhat, S. Arriaga Ramirez, A. M. Rhades, A. Charn, H. I. Diaz, and W. D. Collins, Detection of atmospheric rivers with inline uncertainty quantification: TECA-BARD v1.0.1, *Geoscientific Model Development* **13**, 6131 (2020).
- [41] P. A. Ullrich, C. M. Zarzycki, E. E. McClenny, M. C. Pinheiro, A. M. Stansfield, and K. A. Reed, TempestExtremes v2. 1: A community framework for feature detection, tracking, and analysis in large datasets, *Geoscientific Model Development* **14**, 5023 (2021).
- [42] J. L. Catto and S. Pfahl, The importance of fronts for extreme precipitation, *J. Geophys. Res.: Atmospheres* **118**, 10,791 (2013).
- [43] K. I. Hodges, A general method for tracking analysis and its application to meteorological data, *Monthly Weather Review* **122**, 2573 (1994).
- [44] F. Li, W. D. Collins, M. F. Wehner, and L. R. Leung, Hurricanes in an aquaplanet world: Implications of the impacts of external forcing and model horizontal resolution, *Journal of Advances in Modeling Earth Systems* **5**, 134 (2013).
- [45] T. Berry, D. Giannakis, and J. Harlim, Bridging data science and dynamical systems theory, *Notices of the American Mathematical Society* **67**, 1336 (2020).
- [46] A. Rupe, V. V. Vesselinov, and J. P. Crutchfield, Nonequilibrium statistical mechanics and optimal prediction of partially-observed complex systems, *New Journal of Phys.* **24**, 103033 (2022).
- [47] J. Runge, V. Petoukhov, J. F. Donges, J. Hlinka, N. Jajcay, M. Vejmelka, D. Hartman, N. Marwan, M. Paluš, and J. Kurths, Identifying causal gateways and mediators in complex spatio-temporal systems, *Nature Comms.* **6**, 1 (2015).
- [48] S. Klus, B. E. Husic, M. Mollenhauer, and F. Noé, Kernel methods for detecting coherent structures in dynamical data, *Chaos* **29**, 123112 (2019).
- [49] F. M. Ralph, J. J. Rutz, J. M. Cordeira, M. Dettinger, M. Anderson, D. Reynolds, L. J. Schick, and C. Smallcomb, A scale to characterize the strength and impacts of atmospheric rivers, *Bulletin of the American Meteorological Society* **100**, 269 (2019).
- [50] A. N. Wetzel, L. M. Smith, and S. N. Stechmann, Moisture transport due to baroclinic waves: Linear analysis of precipitating quasi-geostrophic dynamics, *Mathematics of Climate and Weather Forecasting* **3**, 28 (2017).
- [51] E. R. Weeks, J. S. Urbach, and H. L. Swinney, Anomalous diffusion in asymmetric random walks with a quasi-geostrophic flow example, *Physica D* **97**, 291 (1996).
- [52] K. Taira, S. L. Brunton, S. T. Dawson, C. W. Rowley, T. Colonius, B. J. McKeon, O. T. Schmidt, S. Gordeyev, V. Theofilis, and L. S. Ukeiley, Modal analysis of fluid flows: An overview, *AIAA Journal* **55**, 4013 (2017).
- [53] J. H. Tu, C. W. Rowley, D. M. Luchtenburg, S. L. Brunton, and J. N. Kutz, On dynamic mode decomposition: Theory and applications, *J. Comp. Dyn.* **1**, 391 (2014).
- [54] C. Shalizi, Optimal nonlinear prediction of random fields on networks, *DMTCS Proceedings* **vol. AB**, 11 (2003).
- [55] S. Caires and J. A. Ferreira, On the non-parametric prediction of conditionally stationary sequences, *Statistical Inference for Stochastic Processes* **8**, 151 (2005).
- [56] M. M. Bronstein, J. Bruna, Y. LeCun, A. Szlam, and P. Vandergheynst, Geometric deep learning: going be-

- yond Euclidean data, *IEEE Sig. Proc. Mag.* **34**, 18 (2017).
- [57] M. M. Bronstein, J. Bruna, T. Cohen, and P. Veličković, Geometric deep learning: Grids, groups, graphs, geodesics, and gauges, arXiv preprint arXiv:2104.13478 (2021).
- [58] G. Goerg and C. Shalizi, LICORS: Light cone reconstruction of states for non-parametric forecasting of spatio-temporal systems, arXiv:1206.2398.
- [59] H. Jänicke, A. Wiebel, G. Scheuermann, and W. Kollmann, Multifield visualization using local statistical complexity, *IEEE Trans. Vis. Comp. Graphics* **13**, 1384 (2007).
- [60] M. Ester, H.-P. Kriegel, J. Sander, X. Xu, *et al.*, A density-based algorithm for discovering clusters in large spatial databases with noise., in *KDD*, Vol. 96 (1996) pp. 226–231.
- [61] R. Balestrierio and R. G. Baraniuk, Mad Max: Affine spline insights into deep learning, *Proceedings of the IEEE* **109**, 704 (2021).
- [62] N. H. Packard, J. P. Crutchfield, J. D. Farmer, and R. S. Shaw, Geometry from a time series, *Phys. Rev. Lett.* **45**, 712 (1980).
- [63] H. Bénard, *Les Tourbillons Cellulaires dans une nappe Liquide Propageant de la Chaleur par Convection: en Régime Permanent* (Gauthier-Villars, 1901).
- [64] L. Rayleigh, On convection currents in a horizontal layer of fluid, when the higher temperature is on the under side, *Phil. Mag. (Series 6)* **32**, 529 (1916).
- [65] S. Chandrasekhar, *Hydrodynamic and Hydromagnetic Stability* (Oxford, Clarendon Press, 1968).
- [66] F. H. Busse, Non-linear properties of thermal convection, *Reports on Progress in Physics* **41**, 1929 (1978).
- [67] P. Fenstermacher, H. Swinney, and J. Gollub, Dynamical instabilities and the transition to chaotic Taylor vortex flow, *J. Fluid Mech.* **94**, 103 (1979).
- [68] V. Steinberg, G. Ahlers, and D. S. Cannell, Pattern formation and wave-number selection by Rayleigh-Bénard convection in a cylindrical container, *Physica Scripta* **T9**, 97 (1985).
- [69] M. C. Cross and P. C. Hohenberg, Pattern formation outside of equilibrium, *Rev. Mod. Phys.* **65**, 851 (1993).
- [70] W. Heisenberg, Nonlinear problems in physics, *Physics Today* **20**, 23 (1967).
- [71] J. T. C. Liu, Contributions to the understanding of large-scale coherent structures in developing free turbulent shear flows, *Advances in applied mechanics* **26**, 183 (1988).
- [72] H. W. Liepmann, Aspects of the turbulence problem, *Zeitschrift für angewandte Mathematik und Physik ZAMP* **3**, 407 (1952).
- [73] A. A. Townsend, *The structure of turbulent shear flow* (Cambridge university press, 1956).
- [74] J. L. Lumley, The structure of inhomogeneous turbulence, *Atmospheric turbulence and radio wave propagation*, 166 (1967).
- [75] J. C. McWilliams, On the relevance of two-dimensional turbulence to geophysical fluid motions, *Journal de Mecanique Theorique et Appliquee Supplement*, 83 (1983).
- [76] W. S. Parker, Reanalyses and observations: What’s the difference?, *Bulletin of the American Meteorological Society* **97**, 1565 (2016).
- [77] K. Dagon, J. Truesdale, J. C. Biard, K. E. Kunkel, G. A. Meehl, and M. J. Molina, Machine learning-based detection of weather fronts and associated extreme precipitation in historical and future climates, *Journal of Geophysical Research: Atmospheres* **127**, e2022JD037038 (2022).
- [78] T. R. Knutson, J. J. Sirutis, S. T. Garner, I. M. Held, and R. E. Tuleya, Simulation of the recent multidecadal increase of atlantic hurricane activity using an 18-km-grid regional model, *Bulletin of the American Meteorological Society* **88**, 1549 (2007).
- [79] D. R. Chavas, N. Lin, and K. Emanuel, A model for the complete radial structure of the tropical cyclone wind field. Part i: Comparison with observed structure, *Journal of the Atmospheric Sciences* **72**, 3647 (2015).
- [80] NASA, Jupiter cloud sequence from cassini, <https://svs.gsfc.nasa.gov/cgi-bin/details.cgi?aid=3610> (Accessed: 2019-03-14).
- [81] A. Hadjighasem and G. Haller, Geodesic transport barriers in Jupiter’s atmosphere: Video-based analysis, *SIAM Review* **58**, 69 (2016).

Supplementary Information

Methodology

Spatiotemporal Systems

Local causal states are learned representations that extract emergent organization from spatially-extended dynamical systems. The *behaviors* of spatiotemporal systems are *spacetime fields*, elements of the extended phase space that includes time as a dimension. Mathematically, a spacetime field is a tensor $X(\mathbf{r}, t) : \mathbb{S} \rightarrow \mathbb{R}^n$, where \mathbb{S} is some spacetime coordinate system and n is the number of physical field quantities—e.g., temperature, pressure, velocity components, and so on. Each coordinate in spacetime maps to a length- n vector of the values of the physical quantities at that point.

The systems presently analyzed live in a simple Euclidean spacetime, so that $\mathbb{S} = \mathbb{R}^{d+1}$, where d is the number of spatial dimensions. Note though that the spacetime data from the climate reanalysis and Jupiter’s clouds are Euclidean projections from a spherical spatial coordinate system.

Numerical data, with which any data-driven method must necessarily work, will be given on some finite grid \mathbb{G} of dimension (X, Y, T) for two spatial dimensions. The data used here is on a simple integer Euclidean grid (as opposed to a complex adaptive mesh, or spherical grid), so that for each field quantity, $X(\mathbf{r}, t) : \mathbb{G} \rightarrow \mathbb{R}$, where $\mathbb{G} = \{1, \dots, X\} \times \{1, \dots, Y\} \times \{1, \dots, T\}$. As standard, we denote this as $X(\mathbf{r}, t) \in \mathbb{R}^{X \times Y \times T}$.

Loosely speaking, a spatiotemporal system possesses some level of *organization* if many of its degrees of freedom evolve collectively. Coherent structures—the form of organization we are most interested in—implies an emergent higher-level degree of freedom in the system. Particles in a fluid vortex, for instance, will largely travel together through a complex fluid flow. Thus, the particles need not be tracked individually; one can simply track the single vortex [51].

Local Causal States

This motivates the idea of physics-informed representation learning to extract coherent structures. If a spacetime field $X(\mathbf{r}, t) \in \mathbb{R}^{X \times Y \times T}$ is compressed through some encoding, then the encoded representations may leverage the collective organization present in the system. Particularly when representations are learned through an encoder-decoder framework, the collective higher-order degrees of freedom—coherent structures—capture the majority of a system’s behavior and so provide a natural set of compressed representations.

A key distinction between linear modal decompositions [52]—such as POD or the related Dynamic Mode Decomposition [53]—and the local causal states is that modal decompositions provide a finite set of *spatial field templates* (modes). Each spatial mode $\phi(\mathbf{r})$ provides a fixed template with the geometry of a spatial field $X(\mathbf{r})$. The local causal states, by contrast, provide a finite set of *localized templates* that are assigned at each individual point in spacetime.

The locality of local causal states is achieved through the use of *lightcones* in the spatiotemporal system. For systems that evolve according to local interactions, lightcones delineate the causal influence of a point in spacetime. Specifically, the *past lightcone* $L^-(\mathbf{r}, t)$ of a spacetime point $(\mathbf{r}, t) \in \mathbb{S}$ is the set of all spacetime points in the past of (\mathbf{r}, t) that could possibly influence (\mathbf{r}, t) through propagation of the local interactions:

$$L^-(\mathbf{r}, t) := \{(\mathbf{r}', t') : t' \leq t, \|\mathbf{r}' - \mathbf{r}\| \leq c(t' - t)\}, \quad (\text{S1})$$

where c is the speed at which local interactions propagate through the system. Similarly, the *future lightcone* $L^+(\mathbf{r}, t)$ of a spacetime point (\mathbf{r}, t) is the set of all spacetime points at later times that (\mathbf{r}, t) itself can possibly influence through the local interactions, so that:

$$L^+(\mathbf{r}, t) := \{(\mathbf{r}', t') : t' > t, \|\mathbf{r}' - \mathbf{r}\| \leq c(t' - t)\}. \quad (\text{S2})$$

We include the present spacetime point (\mathbf{r}, t) as a member of its past lightcone, but not its future lightcone. See Figure 1.

We denote past and future lightcone random variables as L^- and L^+ respectively, with realizations denoted as ℓ^- and ℓ^+ . Lightcone realizations $\ell^\pm(\mathbf{r}, t)$, or *configurations*, are given by assignment of values from a particular spacetime field $X(\mathbf{r}, t) \in \mathbb{R}^{X \times Y \times T}$ to spacetime points (\mathbf{r}, t) in $L^\pm(\mathbf{r}, t)$.

For systems defined in a discrete spacetime, such as cellular automata [26], the speed of light c is simply given by the radius of local interactions. For systems in a continuous spacetime, like fluid flows, c is given by the speed of sound in the system. As described above in the context of Lagrangian Coherent Structures, we are interested in organization that emerges at advective scales in the flow, which are typically much lower velocities than the speed of sound. In this case, we consider lightcones in the scope of Lagrangian advection, defined by

$$\mathbf{y}(t; t_0, \mathbf{y}_0) := F_{t_0}^t(\mathbf{y}_0) , \quad (\text{S3})$$

where $\mathbf{y}(t)$ represents the spatial position of a fluid particle or tracer at time t .

Consider a fluid particle \mathbf{y} initially at spacetime point (\mathbf{r}_0, t_0) . The trajectory of the particle $\mathbf{y}(t)$, given by the flow map in Eq. (S3), is the solution of the differential equation:

$$\dot{\mathbf{y}} = v(\mathbf{r}, t) , \quad (\text{S4})$$

where $v(\mathbf{r}, t)$ is a smooth velocity field. While the velocity field varies in space and time, we can assign the maximum velocity value v_{\max} so that $v(\mathbf{r}, t) \leq v_{\max}$.

The *Lagrangian lightcones* then are defined by setting $c = v_{\max}$ in Eqs. (S1) and (S2). Again, v_{\max} is typically much smaller than the speed of sound. Lagrangian lightcones capture local causality derived from Lagrangian advection. A Lagrangian past lightcone delineates the possible reach of a particle $\mathbf{y}(t; t_0, \mathbf{y}_0)$ initially at point (\mathbf{r}_0, t_0) through Lagrangian advection in reverse time. That is, all the spacetime points at earlier times from where the particle could possibly have come when evolving according to Lagrangian advection in Eq. (S3). In practice, the value of c used can be seen as a hyperparameter that controls the spatial scale of organization captured by the approximated local causal states. A larger c captures more coarse-grained structures.

In addition to delineating causal influence for points in spacetime, note that lightcones are defined solely in terms of distances in spacetime. This implies that (i) they are *equivariant* under spacetime isometries, such as translations and rotations, and (ii) they are well-defined for any spatial geometry with a distance metric, such as the surface of a sphere or an arbitrary spatial network [54]. Thus, they can be used in a wide variety of spatiotemporal systems, and they transform appropriately under translations, rotations, and reflections. We will return to this later point shortly. Note that planar projections of spherical data, like those we use here for climate data, can break global rotational symmetry, and therefore will not be robust across different projections. However, the local causal states appear to be robust to local rotations in a given projection. For example, the local causal state signature of hurricanes does not change as the hurricane rotates locally.

Having defined lightcones, we can now define local causal states through the *local causal equivalence relation*. Two past lightcone configurations are considered causally equivalent if they have the same conditional distribution over co-occurring future lightcones:

$$\ell_i^- \sim_\epsilon \ell_j^- \iff \Pr(\mathbf{L}^+ | \mathbf{L}^- = \ell_i^-) = \Pr(\mathbf{L}^+ | \mathbf{L}^- = \ell_j^-) . \quad (\text{S5})$$

The equivalence classes of the local causal equivalence relation Eq. (S5) are the *local causal states*. Individual local causal states are denoted ξ and the set of all local causal states for a given system is Ξ .

A local causal state is a set of past lightcone configurations that all have the same conditional distribution $\Pr(\mathbf{L}^+ | \mathbf{L}^- = \ell^-)$. It can also simply be thought of as the conditional distribution itself, since all past lightcone configurations in a local causal state by definition share that one distribution.

Here, we consider deterministic systems whose dynamics do not change over time; e.g., a fluid flow governed by the Navier-Stokes equations with time-independent parameters. Therefore, the conditional distributions over lightcones $\Pr(\mathbf{L}^+ | \mathbf{L}^- = \ell^-)$ are also time-independent—a condition known as *conditional stationarity* [55]. For such systems, each past lightcone configuration ℓ_i^- has a unique and well-defined distribution $\Pr(\mathbf{L}^+ | \mathbf{L}^- = \ell_i^-)$ and, thus, is also associated with a unique local causal state defined by that distribution. Therefore, local causal states do not require the system dynamics to be stationary to be well-defined. This allows us to apply local causal states to conditionally-stationary behaviors, like vortex decay in two-dimensional turbulence.

We define the ϵ -function as the mapping from past lightcone configurations to their corresponding local causal state $\epsilon : \ell^- \mapsto \xi$. The functional form of local causal equivalence relation is given in terms of the ϵ -function as:

$$\ell_i^- \sim_\epsilon \ell_j^- \iff \epsilon(\ell_i^-) = \epsilon(\ell_j^-) . \quad (\text{S6})$$

For a given spacetime field $X(\mathbf{r}, t)$, each spacetime point $(\mathbf{r}, t) \in \mathbb{S}$ has a unique past lightcone configuration $\ell^-(\mathbf{r}, t)$. Applying the ϵ -function then gives a unique local causal state at that point, $\xi(\mathbf{r}, t) = \epsilon(\ell^-(\mathbf{r}, t))$. Therefore, the ϵ -function provides a local point-wise mapping from a spacetime field $X(\mathbf{r}, t)$ to an associated *local causal state*

field, denoted $S(\mathbf{r}, t) = \epsilon(X(\mathbf{r}, t))$). Crucially, the locality of the ϵ -function ensures that a spacetime field $X(\mathbf{r}, t)$ and its associated local causal state field $S(\mathbf{r}, t) = \epsilon(X(\mathbf{r}, t))$ share the same spacetime coordinate geometry \mathbb{S} . For each spacetime point $(\mathbf{r}, t) \in \mathbb{S}$, $X(\mathbf{r}, t) : \mathbb{S} \rightarrow \mathbb{R}^n$ provides the values of the physical variables at that point and $S(\mathbf{r}, t) : \mathbb{S} \rightarrow \Xi$ gives the local causal state $\xi(\mathbf{r}, t) = \epsilon(\ell^-(\mathbf{r}, t))$ at the point.

And so, as promised, the local causal states are local representations assigned to each point (\mathbf{r}, t) in spacetime \mathbb{S} . In this way, the local causal state field $S(\mathbf{r}, t) = \epsilon(X(\mathbf{r}, t))$ provides a *spacetime segmentation* that assigns a local causal state `class label` to each point in spacetime.

The ϵ -function’s locality, together with the equivariance of lightcones under spacetime isometries, implies that the local causal states are also equivariant under spacetime isometries. That is, if g is an isometric transformation (preserves spacetime distances) then it commutes with the ϵ -function: $g \circ \epsilon = \epsilon \circ g$. In the context of coherent structure segmentation, this means that local causal states associated with a particular coherent structure, say hurricanes, do not depend on the hurricane’s spacetime location or orientation. In the Lagrangian Coherent Structure literature, this property ensures local causal states are an *objective* method for coherent structure identification [1, 4]. Analogous to the interpretation of equivariances in neural networks as *geometric deep learning* [56, 57], we can interpret the local causal states as a form of *geometric representation learning* due to their spacetime equivariance and shared coordinate geometry.

Note, too, that locality allows local causal states to capture system structure across scales. All spacetime points associated to a coherent structure may be assigned to a set of local causal states uniquely identifying that structure, independent of the structure’s size [26]. Larger structures simply involve a larger number of spacetime points assigned to those structures’ states.

Similarly, there is no requirement for balanced statistics across occurrences of local causal states. For example, in the results shown here there is often a single local causal state associated with an ambient “background” that occurs most commonly in spacetime, with local causal states associated to coherent structures being relatively rarer.

Finally, we emphasize the local causal state approach’s flexibility. While all examples examined here are on discrete Euclidean spacetimes, the local causal states are well-defined in any spacetime geometry with a distance metric. That said, analyzing large datasets with two spatial dimensions is already computationally taxing, even with large supercomputer resources. In principle, though, the local causal states can be approximated for systems with higher spatial dimensions.

Approximations and Reconstruction

Consider a *data-generating process* \mathcal{P} that produces spacetime fields $X \in \mathcal{P}$ and can either be a natural system or a numerical model. Here, we are interested in real-valued fields, with $X(\mathbf{r}, t) \in \mathbb{R}^n$. Therefore, the spaces of all past and future lightcones for \mathcal{P} , denoted \mathcal{L}^- and \mathcal{L}^+ respectively, are uncountable. Each distribution $\Pr(\mathbf{L}^+ | \mathbf{L}^- = \ell^-)$ is a continuous probability density. Moreover, they are densities conditioned on measure-zero events $\mathbf{L}^- = \ell^-$. There are an uncountable number of past lightcone configurations ℓ^- and, for each of them, there is a conditional density $\Pr(\mathbf{L}^+ | \mathbf{L}^- = \ell^-)$ over an uncountable number of future lightcone configurations.

Thus, in practice approximation is necessary to empirically reconstruct the conditional distributions $\Pr(\mathbf{L}^+ | \mathbf{L}^- = \ell^-)$. Most importantly, we replace the measure-zero past lightcone configurations with something of finite measure. In particular, we partition the space of past lightcones \mathcal{L}^- into finite-measure events $\mathbf{p}^- \in \Sigma_{\mathcal{L}^-}$ for our empirical probability estimates. This allows the following empirical densities to be properly sampled from finite data:

$$\Pr(\mathbf{L}^+ | \mathfrak{P}^- = \mathbf{p}^-) = \int_{\ell^- \in \mathbf{p}^-} \Pr(\mathbf{L}^+ | \mathbf{L}^- = \ell^-) d\mu, \quad (\text{S7})$$

where μ is the data-generating distribution over past lightcones. The finite-measure events partition \mathcal{L}^- , so that $\bigcup_i \mathbf{p}_i^- = \mathcal{L}^-$, $\mathbf{p}_i^- \cap \mathbf{p}_j^- = \emptyset$, and $\mu(\mathbf{p}_i^-) \neq 0$ for all \mathbf{p}_i^- .

To achieve such a finite partitioning, we rely on the *continuous histories assumption* [58, Assumption 3.1] which states that if two past lightcone configurations are similar, they should have similar conditional distributions over future lightcones. Formally, this says that the ϵ -function is continuous over the space of past lightcones, and so $\Pr(\mathbf{L}^+ | \mathbf{L}^- = \ell_j^-) \rightarrow \Pr(\mathbf{L}^+ | \mathbf{L}^- = \ell_i^-)$ as $\ell_j^- \rightarrow \ell_i^-$.

The continuous histories assumption leads us to employ distance-based clustering to create the finite partitioning of the past-lightcone space \mathcal{L}^- . Let $\gamma : \ell^- \mapsto \mathbf{p}^-$ be the mapping from past lightcone configurations to their distance-based cluster element. We refer to individual cluster elements \mathbf{p}^- as *pasts*. The γ -function induces an equivalence

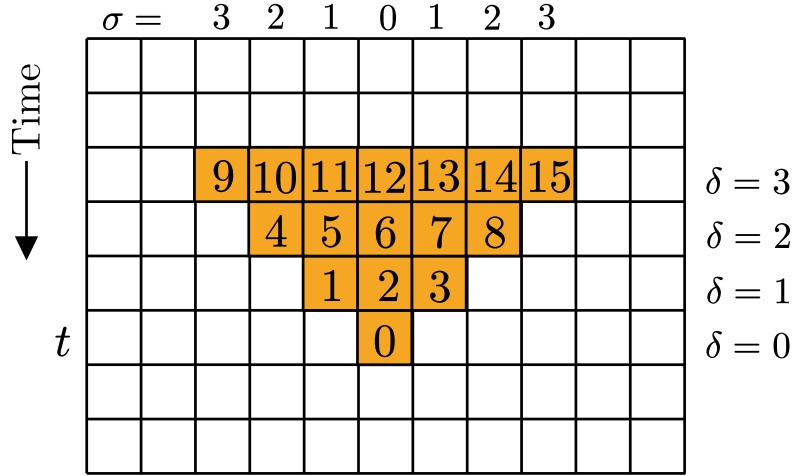


FIG. S1. Finite vector for the past lightcone configuration $\ell^-(\mathbf{r}, t)$ in discrete 1+1 dimensional spacetime with $c = 1$ and finite temporal horizon $h^- = 3$. Overlaid integers indicate the index of that site in the lightcone vector. σ is the space-only internal distance between the base of the lightcone, $i = 0$, and other sites in each vertical column. Similarly, δ is the time-only internal distance for each site in the horizontal row.

relation over past lightcone configurations, similar to the ϵ -function:

$$\begin{aligned} \ell_i^- \sim_\gamma \ell_j^- &\iff \ell_i^- \in \mathbf{p}_a^- \text{ and } \ell_j^- \in \mathbf{p}_a^- \\ \ell_i^- \sim_\gamma \ell_j^- &\iff \gamma(\ell_i^-) = \gamma(\ell_j^-) . \end{aligned}$$

Two past lightcone configurations are γ -equivalent if they are assigned to the same distance-based cluster \mathbf{p}_a^- .

With distance-based γ -equivalence, we state the actionable version of continuous histories our reconstruction algorithm uses as:

$$\gamma(\ell_i^-) = \gamma(\ell_j^-) \implies \epsilon(\ell_i^-) = \epsilon(\ell_j^-) . \quad (\text{S8})$$

That is, if two past lightcone configurations are assigned to the same cluster element from a distance-based clustering, we assume them to be “similar” and so assume that they have the same distribution over future lightcones.

To perform distance-based clustering over lightcones, we need a distance metric on the space of lightcones. First, note that in practice lightcones of finite temporal depth must be used. Individual lightcone configurations are collected into a vector, using a canonical ordering of their elements, up to a finite depth *horizon cutoff* h^\pm in time. Figure S1 shows a past lightcone vector in 1+1 dimensional spacetime with $c = 1$ and $h^- = 3$. Integers overlaid on the lightcone sites indicate the indices of the lightcone vector in the canonical ordering we use.

Prior work [58, 59] used a Euclidean distance over lightcones. In practice with a finite horizon cutoff, this means that values in the lightcone below the cutoff are given a uniform weighting when computing distances, while lightcone values beyond the cutoff are given zero weight. To smooth this step discontinuity, our algorithm uses an exponentially-decaying lightcone distance D_{1c} given as

$$D_{1c}(\mathbf{a}, \mathbf{b}) \equiv \sqrt{(a_0 - b_0)^2 + \dots + e^{-\tau d(l)}(a_l - b_l)^2} , \quad (\text{S9})$$

where \mathbf{a} and \mathbf{b} are length- l finite lightcone vectors, as depicted in Figure S1, and τ is the decay rate.

The decay is applied relative to an internal distance $d(i)$ between the base of the lightcone vector, with index $i = 0$, and other sites in the lightcone with indices $0 < i \leq l$. Figure S1 shows a space-only internal distance as $d(i) = \sigma(i)$ and a time-only internal distance as $d(i) = \delta(i)$. An internal spacetime distance is given as $d(i) = \sqrt{\sigma(i)^2 + \delta(i)^2}$. Results here use the latter spacetime internal distance. This family of exponentially-decaying lightcone distances smooth the step-discontinuity of a simple Euclidean distance by giving less significance to sites in the lightcone that are further away from the present (the base of lightcones).

In addition, the exponential decay has a practical benefit of reducing the effective dimensionality of the lightcone vectors during clustering, as discussed in more detail in Ref. [27]. We use K-Means [28] for our distance-based

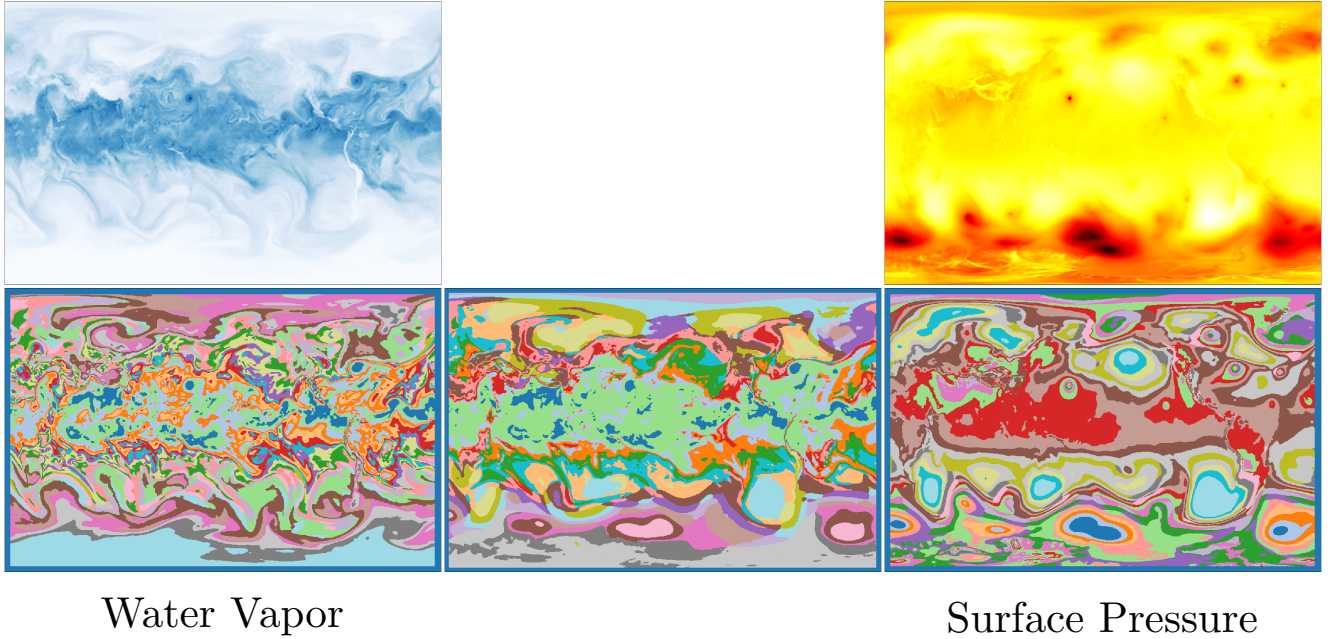


FIG. S2. Local causal state segmentations of TMQ and PSL, with a linear multivariate combined segmentation in between.

clustering of lightcones. Comparison with DBSCAN [60], along with the distributed High-Performance Computing (HPC) implementations of these algorithms, is also given in Ref. [27].

After performing a γ -partitioning of \mathcal{L}^- using K-Means clustering, the densities $\Pr(\mathcal{L}^+|\mathfrak{P}^- = \mathbf{p}^-) = \int_{\ell^- \in \mathbf{p}^-} \Pr(\mathcal{L}^+|\mathcal{L}^- = \ell^-)d\mu$ can be empirically sampled from finite data. To simplify further for our HPC implementation, we also perform a (separate) K-Means clustering over future lightcones to similarly produce finite-measure futures \mathbf{p}_i^+ . This gives a discrete approximation $\Pr(\mathfrak{P}^+|\mathfrak{P}^- = \mathbf{p}_i^-)$ that can be sampled by simple counting. That is, each co-occurring set of pasts $\mathbf{p}_a^- = \gamma^-(\ell^-(\mathbf{r}, t))$ and futures $\mathbf{p}_b^+ = \gamma^+(\ell^+(\mathbf{r}, t))$ are collected in a matrix \mathfrak{P} , where \mathfrak{P}_{ab} is the number of co-occurrences of \mathbf{p}_a^- and \mathbf{p}_b^+ .

With the empirical distributions $\Pr(\mathfrak{P}^+|\mathfrak{P}^- = \mathbf{p}^-)$ we use an empirical approximation to causal equivalence over pasts, rather than over past lightcone configurations. (In principle, the densities $\Pr(\mathcal{L}^+|\mathfrak{P}^- = \mathbf{p}^-)$ can also be used.) If two empirical future distributions are close, according to some empirical test, then their pasts are ψ -equivalent:

$$\begin{aligned} \mathbf{p}_i^- \sim_{\psi} \mathbf{p}_j^- &\iff \Pr(\mathfrak{P}^+|\mathbf{p}_i^-) \approx \Pr(\mathfrak{P}^+|\mathbf{p}_j^-) \\ \mathbf{p}_i^- \sim_{\psi} \mathbf{p}_j^- &\iff \psi(\mathbf{p}_i^-) = \psi(\mathbf{p}_j^-) . \end{aligned}$$

We use hierarchical agglomerative clustering with a chi-squared similarity test ($p = 0.05$) for ψ -equivalence.

Thus, the approximation of the ϵ -function our reconstruction algorithm uses is:

$$\epsilon(\ell^-) \approx \psi(\gamma(\ell^-)) . \quad (\text{S10})$$

Note that because past lightcones of depth 0 reduce to the lightcone base—simply the field value at that point in spacetime—our γ clustering over depth 0 past lightcones reduces to a standard K-Means clustering over the spacetime field. Recent insights into deep learning utilizing maximum affine spline operators [61] shows that trained deep learning models partition their input space, just as under distance-based clustering. This implies “that a D(eep)N(eural network) constructs a set of signal-dependent, class-specific templates” [61], formally similar to local causal state representations. Whereas a neural network uses “ground truth” labels during the supervised learning process to build its templates, the local causal states must be learned in an unsupervised fashion. Our use of lightcones is motivated by weak causality and a local spacetime generalization of delay-coordinate embeddings and their associated intrinsic geometry [62]. This, combined with predictive equivalence, provides the necessary physics of organization [25] with which to extract coherent structures [26].

To reconstruct approximate local causal states for multivariate systems with m physical fields, we aggregate lightcone distances over all the fields. The simplest way to do this is to use the following tensor lightcone metric:

$$D_\ell(\mathbf{a}, \mathbf{b}) \equiv \sqrt{w_0 \left((a_0^0 - b_0^0)^2 + \dots + e^{-\tau d(n)} (a_n^0 - b_n^0)^2 \right) + \dots + w_m \left((a_0^m - b_0^m)^2 + \dots + e^{-\tau d(n)} (a_n^m - b_n^m)^2 \right)}.$$

A practical advantage of this particular metric is that it can be achieved by simply concatenating the scalar lightcone vectors taken from each field. Empirically, we observe that this metric yields a local causal state field that is a weighted interpolation of the component fields, with relative weighting given by the coefficients w_i . We use the water vapor and surface pressure fields of the CAM5.1 model to demonstrate this.

From visual inspection, signatures of hurricanes can be seen in the column-integrated water vapor field (TMQ) and surface pressure field (PSL), among others. Running local causal state segmentation on these fields alone is not sufficient for producing a unique segmentation class corresponding to hurricanes. The segmentation class of the TMQ field corresponding to hurricanes also shows up in the tropics in regions of high water concentration, which are not hurricanes. Similarly, the PSL segmentation class corresponding to hurricanes shows up in similar, but larger scale, pressure patterns in the extra tropics (particularly in the southern hemisphere).

Figure S2 gives example segmentations of these fields. The middle of Figure S2 shows a multivariate segmentation incorporating both fields, with the PSL field given $\frac{1}{4}$ the weight of TMQ in the lightcone tensor metric described above. Qualitatively, one sees how clustering with this metric produces a weighted interpolation between segmentations of the two fields separately. In this case, the tropics and northern hemisphere are more reflective of the TMQ field, while the southern hemisphere is more reflective of the PSL field. Unfortunately, interpolating features from both fields together does not result in the desired unique hurricane segmentation class.

Application Problems and Data Sets

Turbulence

The formal study of emergent organization had its genesis with Bénard’s work [63] on the spontaneous formation of fluid convection cells [64–68] at the turn of the 20th century. Around the same time, the dawn of quantum mechanics took prominence in fundamental physics. Even up to the present, however, fluid turbulence has remained lingering as “the last mystery in classical physics”. Arguably, the primary “mystery” is that of emergent organization [69], with turbulence being the flagship instantiation [70].

The importance of secondary large-scale coherent structures in general theories of turbulence was recognized in the latter half of the 20th century, as documented in Ref. [71]. The first exploration of turbulent coherent structures were statistical in nature. It was observed that turbulence has a statistical separation of scales in fluctuations about the mean flow. There are smaller, fine-scaled “random” fluctuations on top of larger “not random” fluctuations, the latter being identified as coherent structures [71]. This statistical organization was identified and corroborated through characteristic signatures in the correlation function [72, 73].

Structural approaches, rather than statistical, appeared later, particularly with the introduction of the Proper Orthogonal Decomposition in the study of turbulence [74]. The POD approach follows an Eulerian paradigm, viewing the full spatial fields as the state of a spatially-extended dynamical systems. The spatial fields are then decomposed into POD modes, which have an optimality property that the leading modes capture the dominant contributions to kinetic energy. A (relatively) low-dimensional dynamical system analysis of the evolution of the POD modes provides an analysis of the flow in terms of its dominant *energetic* coherent structures [2].

Also building on ideas and tools from low-dimensional dynamical systems, the geometric theory of coherent structures follows the Lagrangian paradigm. Rather than seeking to capture energetically-dominant structures, the Lagrangian approach seeks coherent structures that organize advective transport in the flow. Lagrangian coherent structures are thus found as the most attracting, repelling, or shearing material surface in the flow [1].

The local causal states are a general representation learning method like POD. However, when applied to fluid flows using Lagrangian lightcones, as described above, they are more closely related to Lagrangian coherent structure approaches.

To analyze the ability of local causal states to capture fluid coherent structures we examine vortex dynamics in two-dimensional turbulence. This particular flow is ideal for several reasons. First, it is two-dimensional, making it

easier to analyze with computationally expensive algorithms. However, unlike simple two-dimensional flows like von Kármán vortex streets, the two-dimensional turbulent flow supports behaviors characteristic of anisotropic turbulence in three dimensions, particularly in geophysical flows [75].

Second, the coherent structures that emerge in two-dimensional turbulence—coherent vortices—are paradigmatic fluid coherent structures. Moreover, while a general theory of the emergent vortex dynamics remains elusive, the dynamics are known empirically and are qualitatively simple. Two like-signed vortices, under the right conditions, will pairwise merge when they are close enough. Third, this pairwise merging behavior results in a power-law decay of the total number of vortices in the flow over time [31, 32]. Identification of the power-law decay provides a quantitative metric to test potential vortex coherent structure detection methods. Note that the identification of the “theoretical” range for the decay rate $\nu = -(0.71 - 0.75)$ is identified using a specialized vortex identification algorithm based on vorticity thresholding along with geometric considerations [31].

We use data generated from the Fluid2D solver publicly available on GitHub (https://github.com/pvthinker/Fluid2d/tree/master/experiments/TwoDim_turbulence). The local causal state segmentation used to count vortex cores, shown in Figure 2 (b), uses the following parameters: past lightcone horizon 14, future lightcone horizon 2, propagation speed $c = 1$, $K = 3$ for past lightcone K-Means, $K = 25$ for future lightcone K-Means, and a spacetime decay with decay rate $\tau = 0.25$ for the lightcone distance metric.

Climate

While spacecraft allow for direct video observations of portions of the atmosphere, similar to that of Jupiter shown below, direct observations of the relevant physical fields of the full atmosphere are not possible. Numerical models are used to aggregate inhomogeneous data sources and create *data images* of the physical fields most consistent with the observations [11]. This process is known as *reanalysis* and represents the closest one can come to “true” observational climate data [76].

In contrast to reanalysis data, general circulation models (GCM) simulate the dynamics of the atmosphere to make short-term predictions (e.g., numerical weather prediction) and long-term climate forecasts. Long-term forecasts are the key tool for analyzing the potential future impacts of global warming [11, 13]. Tools such as the local causal states provide an enhanced level of analysis to answer detailed questions, such as how the intensity and dynamics of extreme weather events will change under different warming scenarios.

In this study, we use data from the historical calibration run of the high resolution 0.25° CAM5.1 GCM [36]. Single-precision climate variables are stored on an 1152×768 spatial grid, with a temporal resolution of 3 hours. The segmentation results shown here use data from the autumn of 2015 of the CAM5.1 historical run 1. The physical fields used for the various local causal state segmentation results are the column-integrated water vapor (TMQ), the near-surface velocity components (U850) and (V850), as well as the integrated vapor transport (IVT) field, defined as:

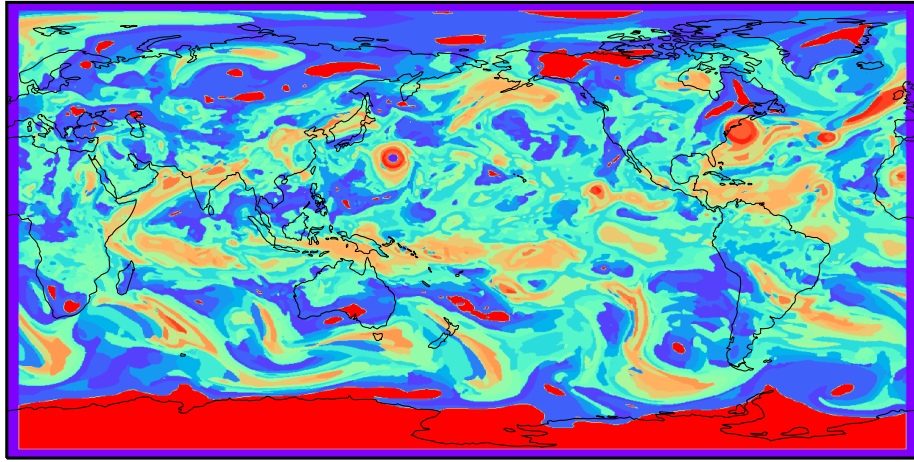
$$\left[\left(\frac{1}{g} \int_{1000hPa}^{600hPa} qu \, dp \right)^2 + \left(\frac{1}{g} \int_{1000hPa}^{600hPa} qv \, dp \right)^2 \right]^{1/2},$$

where here q is water vapor, u and v are wind velocity components, and p is pressure.

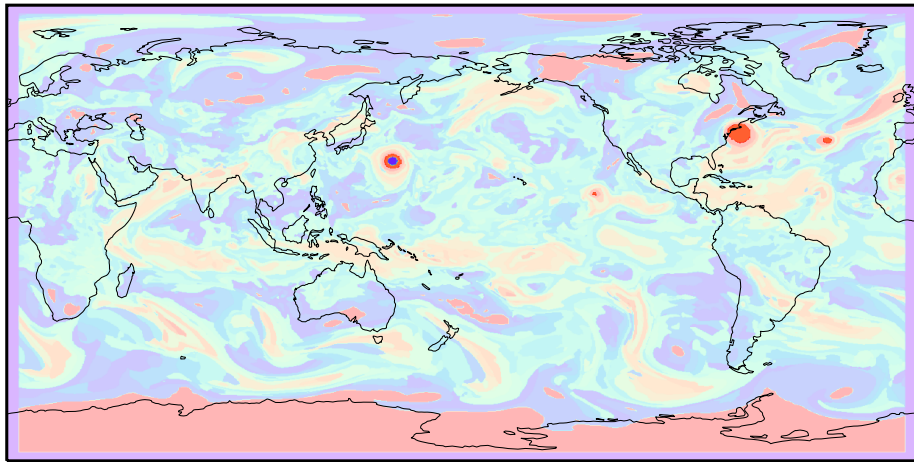
Hurricane Tracker

We create a hurricane tracker using a univariate local causal state segmentation of the IVT field, as shown in Figure S3. A snapshot of the local causal state field $S(\mathbf{r}, t)$ from this segmentation is shown in (a). From visual inspection, we find a particular set of **hurricane** states that seem to co-occur with hurricanes. That is, it appears that (almost) all spacetime points (\mathbf{r}, t) such that $S(\mathbf{r}, t)$ is one of the **hurricane** states are points where a hurricane is present (as seen in the TMQ field). The **hurricane** states are highlighted in the local causal state segmentation of Figure S3 (b). To aid the visual identification of the **hurricane** states with actual hurricanes, a snapshot of the water vapor field (TMQ) is shown in (c) with spacetime points (\mathbf{r}, t) , such that $S(\mathbf{r}, t)$ is one of the **hurricane** states, given a red mask overlaid on top of the vapor field. We emphasize again that this is possible due to the shared coordinate geometry of the physical fields and the local causal state field.

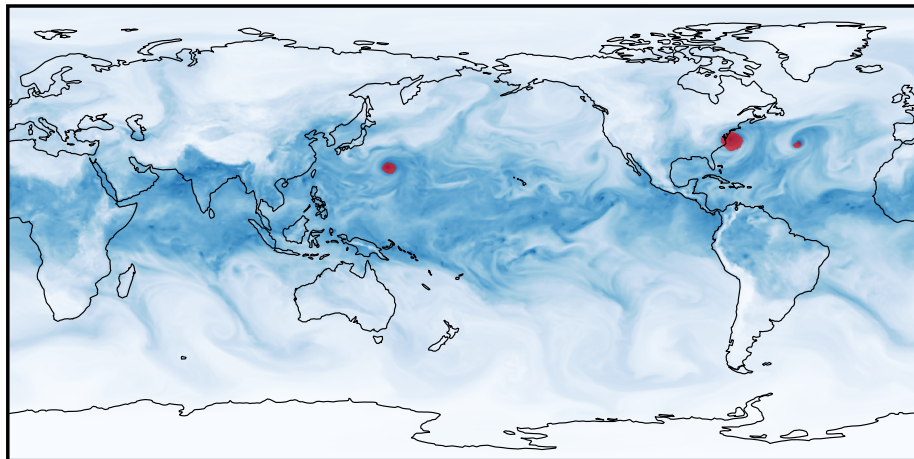
The local causal state segmentation of the IVT field, shown in Figure S3, was created using the following parameters: past lightcone horizon 16, future lightcone horizon 3, propagation speed $c = 1$ (one spatial grid cell per single 3-hour



(a) Local causal state segmentation of IVT field



(b) hurricane local causal states highlighted



(c) hurricane states overlaid on top of water vapor field

FIG. S3. Creation of hurricane tracker using local causal state segmentation of the IVT field.

time step), $K = 24$ for past lightcone K-Means, $K = 50$ for future lightcone K-Means, and decay rate $\tau = 1.0$ for the lightcone distance metric.

General Extreme Weather Events

The more general extreme weather local causal states shown in Figure 3 (a) are produced using a multivariate segmentation that combines the TMQ, U850, and V850 vapor and velocity fields using a tensor lightcone metric based on IVT,

$$D_{\text{lc}}(\mathbf{a}, \mathbf{b}) \equiv \sqrt{\left((a_0^q a_0^u - b_0^q b_0^u)^2 + \dots + e^{-\tau d(n)} (a_n^q a_n^u - b_n^q b_n^u)^2 \right) + \left((a_0^q a_0^v - b_0^q b_0^v)^2 + \dots + e^{-\tau d(n)} (a_n^q a_n^v - b_n^q b_n^v)^2 \right)}. \quad (\text{S11})$$

Here, \mathbf{a} and \mathbf{b} are lightcone tensors such that lower indices are the lightcone locations (as shown in Figure S1) and upper indices are the physical fields; q is water vapor, and u and v are the near-surface velocity components. Using this metric, the local causal state segmentation shown in Figure 3 (a) is reconstructed using the following parameters: past lightcone horizon 6, future lightcone horizon 3, propagation speed $c = 2$, $K = 14$ for past lightcone K-Means, $K = 20$ for future lightcone K-Means, and spatiotemporal decay rate $\tau = 0.5$.

As described above, the non-white states in Figure 3 (a) represent general coherent structures, according to the local causal state definition [26], that we hypothesize correspond to extreme weather events (EWEs). These include known structures like hurricanes and atmospheric rivers, as well as additional as-of-yet unknown structures. To test the relevance of these structures (particularly the unknown ones) to weather extremes, we examine their relation to precipitation extremes using the PRECT 3 hour cumulative precipitation field of the CAM5.1 model. Note that PRECT is not used to reconstruct the EWE local causal states.

We follow a similar procedure as Reference [77], which uses supervised deep learning to track fronts and associate precipitation extremes with the identified fronts. Here, we count the number of global precipitation extremes that co-occur with the EWE local causal states (the non-white states in Figure 3 (a)). That is, we find the spacetime locations (\mathbf{r}, t) of all extreme precipitation events of a given percentile and check to see if $S(\mathbf{r}, t)$ is one of the EWE states. If so, the extreme precipitation event co-occurs with the EWE local causal states. Results are shown above in Table I.

TECA Details

TECA [22] is a software package that provides a unified platform for extreme weather and climate analytics. The results shown in this work use two distinct heuristics, one for hurricanes and one for ARs, both implemented in TECA.

TECA hurricane segmentation follows the TSTORMS code, originally developed by the Geophysical Fluid Dynamics Laboratory and described in Ref. [78]. In this, explicit physical thresholds are set to determine hurricanes as local maxima of vorticity and temperature, and local minima of pressure. Implemented with the command line function `teca_tc_detect`, this algorithm identifies hurricane centers. We use the default settings for this function.

Complete hurricane segmentation is achieved by including wind radius information [79]. This uses wind radial profiles that define category strengths of hurricanes. We wish to be as unrestrictive as possible in identifying possible EWEs with TECA, so we use the “category 0” wind profile, which gives the largest storm radius, provided by the command line function `teca_tc_wind_radii`. That is, each hurricane center provided by `teca_tc_detect` has an associated “category 0” wind radius given by `teca_tc_wind_radii` that provides the size of the category 0 hurricane at each time. This common hurricane segmentation approach necessarily gives hurricanes with circular shapes, whereas the local causal states do not have such explicit shape constraints.

AR segmentation is performed separately from hurricane segmentation using the TECA-BARD algorithm [40]. In this, a standard AR heuristic is first employed that detects candidate ARs from the integrated vapor transport (IVT) field based on threshold, size, and location. A Bayesian framework is then applied to tune the specific parameters (e.g., the hard threshold) of this heuristic to best match the AR segmentation from a small dataset hand-labeled by climate experts [23]. The output of TECA-BARD is an AR likelihood, which gives the probability of the presence of an AR at each spacetime point. To create a binary AR segmentation with ARs either present or not, we use a likelihood threshold of $2/3$.

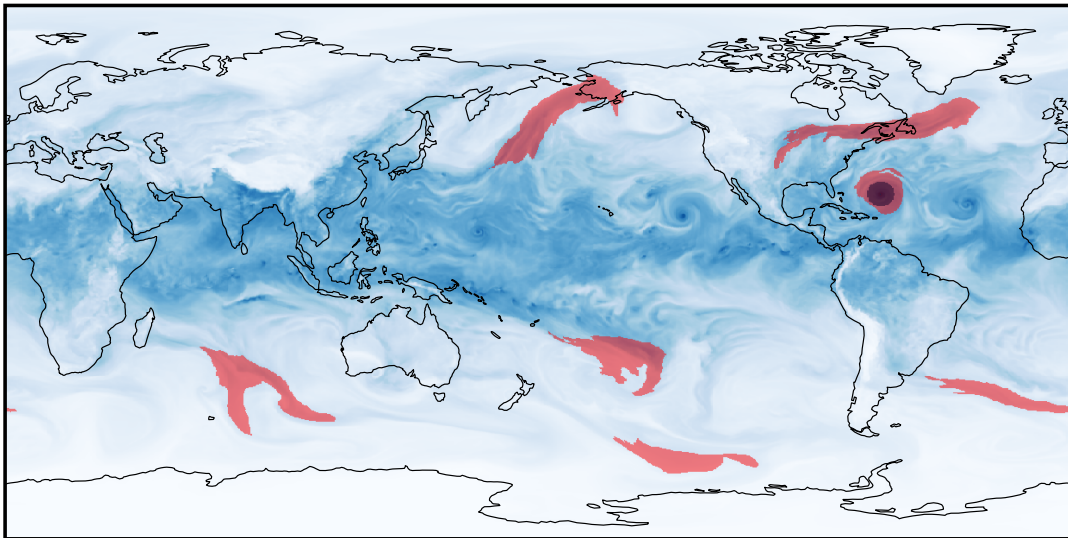


FIG. S4. TECA AR heuristic false identification of a hurricane as an AR.

Since heuristics such as TECA are not ground-truth, they may produce false event detections. A clear example is shown in Figure S4, in which TECA-BARD misidentifies a hurricane off the east coast of North America as an AR. The light red colors in Figure S4 are AR segmentation labels from TECA-BARD. The darker-colored circle is the distinct **hurricane** TECA segmentation, again performed entirely separately from TECA-BARD. Thus, spacetime points inside the dark circle are labeled as **hurricane** by the TECA hurricane heuristic and also labeled as **AR** by the TECA-BARD AR heuristic.

The TECA codebase is developed and maintained by LBNL and is publicly available on GitHub: <https://github.com/LBL-EESA/TECA>.

Complexity and Symmetry Breaking: Clouds of Jupiter

We close by examining several local causal state segmentations of the clouds of Jupiter. These examples compare the effects of various inference parameters on the resulting segmentation and serve to illustrate the idea of increasing complexity through symmetry breaking.

Figure S5 shows the results with the observable grayscale image of Jupiter’s clouds, taken from the NASA Cassini spacecraft [80], shown in (a). The largest scale structures that appear are the east-west zonal bands separated by strong jet streams [81]. To capture this large scale structure, we first perform a segmentation using a (relatively) large speed of light for the lightcones $c = 4$. (Memory requirements of the algorithm scale most rapidly with c). This effectively provides a larger spatial convolution kernel with each lightcone and thus averages over the smaller scale degrees of freedom within that kernel. The result, shown in (b), provides segmentation classes that follow the large scale structure and zonal bands. In addition, the boundaries between classes corresponding to the zonal bands identify the east-west jet streams that separate the bands.

To capture more smaller-scale detail, particularly at the boundaries of zonal bands, the segmentation in (c) uses the exact same parameters as (b), but includes a nonzero spatial decay in its lightcone metric. This decay effectively reduces the size of the spatial convolution kernels and so captures smaller scale detail. Most noticeable is the appearance of the “string of pearls” in the southern hemisphere that are much more clearly outlined in (c) than in (b). Note that the different spatial scales found between (b) and (c) could not be recovered using a standard K-Means segmentation; K is set to 3 for both cases, only the spatial decay rate differs.

While decreasing the (effective) size of the spatial kernel reveals smaller scale details at zonal band boundaries, we can see from (a) that there is additional turbulent structure within the bands themselves. The segmentation in (d) reveals more of this internal structure by decreasing the size of the spatial kernel further using $c = 1$ and increasing the number of segmentation classes found; i.e., increasing K in K-Means. The increased complexity corresponds to

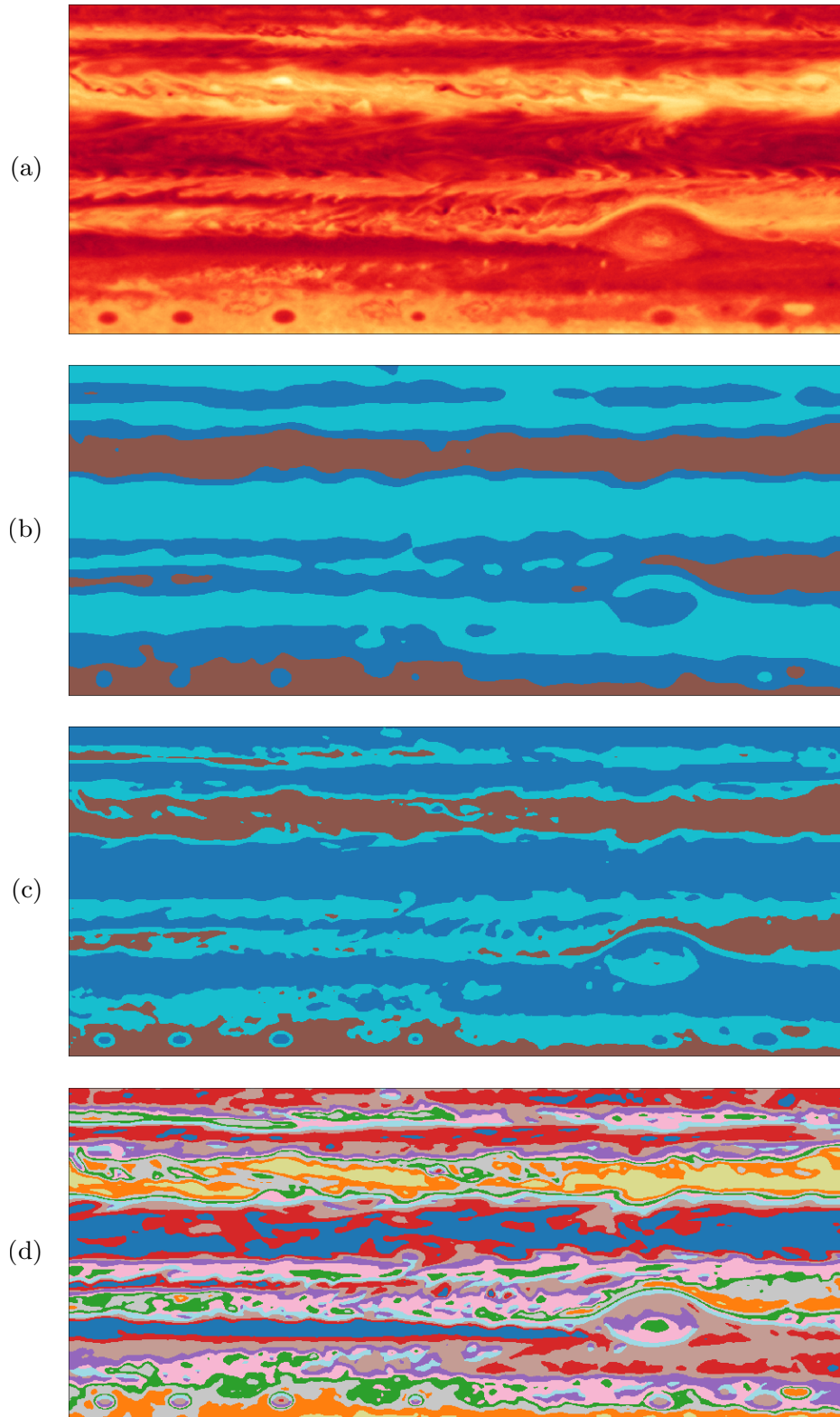


FIG. S5. Suite of local causal state segmentations (b)-(d) of Jupiter's clouds (a).

system’s broken symmetries, reminiscent of the bifurcation theory of pattern formation. That is, points within a zonal band belong to the same segmentation class in (b), signaling they are part of the same large scale structure. However, they may correspond to different classes in (d), identifying the points belong to different structures at smaller scales. The separation of scales then represents an elevated level of complexity in the system’s spatial structure—a coexistence of organization and chaos (turbulence).

Note that in all segmentation analyses the local causal states vary more in the vertical direction of the images than the horizontal. As mentioned, the east-west horizontal bands are the most prominent structures in Jupiter’s atmosphere, created by strong jet streams that act as transport barriers. We again emphasize that Lagrangian Coherent Structures and our local causal state approach using Lagrangian lightcones discover coherent structures associated with material transport. It is not surprising then that local causal states are extended in the east-west direction following the zonal banding. Particularly evident in the coarse-grained segmentation shown in (b), the north-south boundaries between two local causal state bands then indicate the presence of a jet that acts as a transport boundary between the bands.

CODE AVAILABILITY

Supporting Python source code, SLURM run scripts, parameter logs, and Jupyter notebooks displaying results and figures can be found at <https://github.com/adamrupe/Emergent-Organization>.

AUTHOR CONTRIBUTIONS

AR and JPC developed the theoretical framework; KK, AR, and JPC conceptualized the problem applications; AR and KK performed the application experiments and analysis; AR wrote the prototype code; NK and AR wrote the distributed HPC code; AR and JPC wrote the manuscript.

ACKNOWLEDGMENTS

The authors thank Vladislav Epifanov, Oleksandr Pavlyk, Frank Schlimbach, Mostofa Patwary, Sergey Maidanov, and Victor Lee for their help in developing the HPC implementation of local causal state reconstruction. We thank Nicolas Brodu, Jian Lu, Anastasiya Salova, and Mikhael Semaan for helpful comments and feedback. We also thank Michael Wehner for providing the IVT fields of the CAM5.1 data, Burlen Loring for help implementing TECA hurricane segmentation, Travis O’Brien for sharing TECA AR segmentation, Wahid Bhimji for help with NERSC resources, and Prabhat initiating and leading the collaboration Project DisCo that ultimately led to the results in this work.

Part of this research was performed while AR was visiting the Institute for Pure and Applied Mathematics, which is supported by the National Science Foundation grant DMS-1440415. AR acknowledges the support of the U.S. Department of Energy through the LANL/LDRD Program and the Center for Nonlinear Studies. JPC would like to acknowledge Intel[®] for supporting the Intel Parallel Computing Center at UC Davis. KK was supported by the Intel[®] Big Data Center. This research is based upon work supported by, or in part by, the U. S. Army Research Laboratory and the U. S. Army Research Office under contracts W911NF-13-1-0390 and W911NF-18-1-0028, and the U.S Department of Energy (DOE), Office of Science, Office of Biological and Environmental Research, **Earth and Environmental Systems Modeling program**. This work used resources of the National Energy Research Scientific Computing Center, a DOE Office of Science User Facility supported by the Office of Science of the U.S. Department of Energy under Contract No. DE-AC02-05CH11231. The Pacific Northwest National Laboratory (PNNL) is operated for DOE by Battelle Memorial Institute under contract DE-AC05-76RLO1830.